CHARACTERIZATION OF INHERENT AND INDUCED ANISOTROPY IN GRANULAR MATERIALS

CHARACTERIZATION OF INHERENT AND INDUCED ANISOTROPY IN GRANULAR MATERIALS

BY

MARJAN OBOUDI, M.SC., B.SC.

A thesis

Submitted to the School of Graduate Studies in Partial Fulfillment of the Requirements for the Degree

Doctor of Philosophy

McMaster University

DOCTOR OF PHILOSOPHY (2014) **McMaster University**
Hamilton, Ontario

TITLE: **Characterization of Inherent and Induced Anisotropy in Granular Materials**

AUTHER: **Marjan Oboudi**
M.Sc., B.Sc., Shiraz University,
Shiraz, Iran

SUPERVISORS: **Professor S. Pietruszczak**
Professor A. G. Razaqpur

NUMBER OF PAGES: xv, 120

To My Mom and Dad

&

Ashkan

Thanks for always being there for me

ABSTRACT

The main aim of this PhD dissertation is to investigate the inherent and induced anisotropy in granular materials. The study includes both the experimental and theoretical aspects and provides a methodology for characterizing the mechanical response of granular materials that display anisotropy.

The content of this thesis is divided into two main parts. The first part is focused on investigating the mechanical properties of materials with inherent anisotropy. In particular, an experimental program designed to investigate the mechanical properties of Ottawa standard sand (C109), with inherent anisotropy that is generated by the initial densification process, is described. The program involves a series of direct shear as well as triaxial axial tests. Its primary objective is to demonstrate that anisotropy may occur in sands that have nearly spherical particles (i.e. are typically considered as isotropic) provided the distribution of pore space has a preferred orientation due to the initial densification process. Following the experimental part, the mathematical formulation based on the Critical Plane Approach (CPA) is presented for describing anisotropic mechanical behavior of the material. The procedure for identification of parameters embedded in the constitutive model is outlined and an extensive numerical analysis is conducted simulating the experimental tests.

The second part of this thesis deals with induced anisotropy and its focus is on developing an evolution law for the fabric of particulate materials as a function of

continuing deformation. The microstructure descriptors are based on lineal intercept measurements and include the areal porosity and the mean intercept length distribution. The methodology involves performing a series of Discrete Element simulations for a granular assembly under evolving directions of the principal stress/strain and defining a correlation with the evolution of material axes. It is demonstrated that granular materials with spherical particles may become anisotropic due to the initial compaction process and that the induced anisotropy is characterized by the coaxiality between the microstructure and the total strain tensors. The proposed evolution law is incorporated into the constitutive framework for anisotropic materials, as discussed in the first part of this thesis, and some numerical simulations are conducted. It is demonstrated that the proposed approach can describe, at least in a qualitative manner, several manifestations of induced anisotropy in granular materials.

ACKNOWLEDGMENTS

I am deeply grateful to my supervisor, Dr. Stan Pietruszczak, for his continuous support and guidance throughout my PhD. I am equally indebted to my co-supervisor, Dr. Ghani Razaqpur, for his valuable comments and encouragement to improve my work.

I would like to thank my PhD committee members, Dr. Peijun Guo and Dr. Peidong Wu for their insightful comments and discussions.

I would also like to acknowledge the financial support of the Department of Civil Engineering at McMaster.

In special, I am thankful to my husband, my parents, my sister and brothers, and my lovely nephew, Arsham, who made several sacrifices that allowed me to pursue my PhD.

TABLE OF CONTENTS

TABLE OF ILLUSTRATIONS

LIST OF TABLES

CHAPTER 1. INTRODUCTION

1.1. Anisotropy in geomaterials

Many geomaterials such as sedimentary rocks and soils exhibit significant inherent anisotropy. In this case, both the deformation response and the failure mode are strongly dependent on the loading orientation with respect to their microstructure. Furthermore, the mechanical behavior of geomaterials is also sensitive to changes in the internal structure due to imposed deformation and/or environmental effects (e. g. reduction or increase in geostatic stress field, temperature changes, variations in the chemical composition of pore water and water content). Thus there is a coupling between induced and inherent anisotropy which will affect failure mechanisms and deformation characteristics in these materials. The description of induced anisotropy is, in general, more difficult than the inherent one. This stems mainly from the fact that in inherently anisotropic materials the principal material directions are known *a priori*, while for induced anisotropy a specific measure of fabric is required in order to quantify its evolution during the loading process. Over the last few decades, extensive studies have been carried out to investigate the anisotropy effects in geomaterials. In what follows a brief review of both experimental and theoretical investigations is provided.

1.1.1. Review of experimental investigations

In order to investigate the anisotropic strength-deformation characteristic of a geomaterial one must allow for the rotation of principal stress directions, relative to the axes of material symmetry. In early experiments pertaining to the anisotropy of overconsolidated clays, the rotation of principal material axes was achieved by extracting specimens at different inclinations with respect to the major consolidation stress or the direction of the deposition and subsequently compressing it in a conventional triaxial cell (Mitchel 1972). It is worth noting that the conventional triaxial tests were also used to investigate induced anisotropy, in particular the effects of large drained pre-shearing on the response of dense sand (e. g. Poorooshasb et al. 1966 and 1967, Tatsuoka and Ishihara 1974, Ishihara and Okada 1978 and 1982) as well as loose sands (e.g. Lanier et al. 1993, Doan et al. 1997, Vaid et al. 1989). The experimental data revealed the important role of drained preloading histories on the undrained shear strength of sands. More recently, the influence of previous deviatoric strain histories on the undrained behaviour of loose sands was investigated in a series of papers by Doanh et al. (2010, 2012 and 2013). Starting from an initially isotropic or anisotropic stress state, different deviatoric strain histories were generated by a standard drained pre-sheared cycle up to a specified stress ratio. Analysis of the experimental results indicates a progressive transformation of the usual contractive and unstable behavior of loose sand into a dilative

and stable behaviour of dense like sand, while remaining within a narrow range of loose density. In a conventional triaxial apparatus only the normal and parallel orientations of the major applied stresses relative to the axes of material symmetry can be achieved. Arguments have been made regarding the testing of samples inclined at intermediated angles. The argument is based on the fact that for inclined specimens the distortion is constrained by the presence of loading platens, which leads to non-uniformity in the resulting stress field. Note that several investigators conducted extensive triaxial experiments on inclined samples (e.g., Duveau et al. 1998, Oka et al. 2002); however the quantitative conclusions in terms of the spatial variation of strength, are questionable.

In order to more accurately examine the main features of anisotropy in geomaterials, other types of testing equipment have been developed, including directional shear cell and hollow cylinder apparatus. In these tests, a controlled rotation of principal stress directions is possible and moreover, the effect of intermediate principal stress can be either controlled or monitored.

In directional shear apparatus the direction of the major principal stress is controlled by varying the normal and shear stress acting on four surfaces of a cubical sample placed between the rigid end platens. During the test, the detailed information about strain distribution is provided by recording either the surface displacement field or the radiographic-photographic tracing of the shot displacements embedded in a specimen. A series of directional shear tests performed by Jamiolkowski et al. (1985), on loose sand

and resedimented clay, indicated the sensitivity of elasto-plastic response and shear strength to the directions of principal stresses relative to the symmetry axis of material. Another interesting study illustrating the influence of the strain induced anisotropy was conducted by Wong and Arthur (1985). A series of drained tests were carried out on the specimen of loose sand, initially pre-strained in shearing with a fixed major principal stress direction. Subsequently the specimen was unloaded and repeatedly sheared with a major principal stress fixed in a different direction. The strain induced anisotropy resulted in stiffer response at small rotation angles and softer one at higher rotation angles. Furthermore, it was demonstrated that inherent anisotropy generates a continuous degradation in stiffness as the direction of major principal stress rotates from 0° to 90°. On the other hand, the strain induced anisotropy reduces stiffness to a minimum at the rotation of about 70° and then it results in progressive increase. Similar effects were also observed in experiments on dense sands (Arthur et al. 1977 and 1981).

In a hollow cylinder apparatus the combinations of axial and torsional stresses leads to principal stresses that are inclined with respect to the axes of symmetry of the material. Over the last few decades, extensive studies have been carried out on the effects of principal stress rotation on the response of geomaterials. These included the tests on sands (e. g. Lade 1981, Sivathayalan and Vaid 2002, Symes et al. 1984 and 1988, Vaid et al. 1990, Yang et al. 2007) as well as clays (e. g. Hicher and Lade 1987, Hong and Lade 1989, Nishimura et al. 2007, Saada et al. 1994). Recently, a comprehensive study on the behavior of sand specimens, employing hollow cylinder apparatus, was reported by Lade

et al. 2013. The results of a large series of tests on dense fine Nevada sand deposited with horizontal bedding planes were presented which indicated a considerable dependence of the friction angle on the direction of the major principal stress relative to vertical, α. The friction angles were shown to be highest for $\alpha = 0^{\circ}$ and all b-values[1]. The strength was lowest values for $\alpha = 67.5^{\circ}$ at which the major principal stress is inclined such that the potential shear band directions coincide with the bedding planes. Within the full range of b and $\alpha-$values, the friction angle varied from 57° to 32° while the friction angle from a conventional triaxial compression test on a vertical specimen was 41°.

1.1.2. Review of theoretical investigations

Over the last few decades, several constitutive models have been developed that are capable of reproducing some aspects of soil anisotropy under a variety of loading conditions. Iwan (1967) and Mroz (1967) independently introduced the concept of multisurface kinematic hardening by including a set of nested yield surfaces that translate in stress space. This concept was initially developed for metals but quickly found applications in modeling of geomaterials. For example, Prevost (1977, 1978) expanded the concept of nested surfaces in a generalized multisurface plasticity framework. In this

[1] b-value indicates the relative magnitude of the intermediate principal stress, expressed as $\sigma_2 - \sigma_3/\sigma_1 - \sigma_3$.

model the inherent anisotropy of the material was addressed by specifying the initial location of the surfaces before the beginning of loading process. It should be noted that the framework of kinematics hardening is, in general, restrictive and cannot describe the directional effects which are associated with any form of anisotropy.

A more rigorous approach to model anisotropy is based on introducing a fabric tensor. In this approach, constitutive models are generally formulated in terms of tensorial variables characterizing the state of the microstructure, together with or independently from the evolution laws for the state variables. Boehler and Sawczuk (1977) developed a general form of the yield criterion as a function of ten independent invariants of stress and fabric tensors. A simplified and more pragmatic approach was developed by Pietruszczak and Mroz (2000) who introduced a scalar anisotropy parameter that is function of mixed invariants of stress and microstructure orientation tensors. They also developed a general form of the Critical Plane approach in which the strength properties are assumed to be orientation-dependent. In earlier work, Krucinski and Pietruszczak (1989) developed a mathematical framework for describing the induced anisotropy in clays. The framework employs the concept of an "equivalent continuum" and introduces a measure of material fabric which is defined as an implicit function of the spatial distribution of porosity/void ratio. Anisotropy has also been modeled by a "multilaminate model" in which plastic slip occurs on generic planes in the material (Zienkiewicz and Pande 1977, Pande and Sharma 1981, Pande and Xiong 1982, Pietruszczak and Pande 2001). A similar model with slip occurring on a set of predefined

microplanes was developed by Bazant and Prat (1987) and modified by Bazant et al. (2000) and by Carol et al. (2001). Lydzba et al. (2004) developed a mathematical framework for modeling the time-dependent creep phenomenon in frictional materials exhibiting a strong inherent anisotropy, which incorporated a scalar anisotropy parameter. The creep was assumed to be associated with progressive rearrangement of material structure. The description of plastic deformation and damage in sedimentary rocks, with emphasis on coupling between inherent and induced anisotropies, was investigated by Chen et al. (2012).

1.1.3. Correlating the internal structure and the macroscopic response

Establishing a correlation between the internal structure and mechanical characteristics of geomaterials is a non-trivial task. Various measures of internal structure have been employed in the past, including the distribution of grain contact normals (particulate media, Oda 1972), crack orientations (rock mass, Kanatani 1985) etc. Clearly, the definition of a fabric tensor is not unique as different measures of microstructure may be adopted leading to different correlations with mechanical properties. It is important, however, that any chosen measure be experimentally identifiable. Therefore, the preference here may be given to descriptors that can be determined by means of known stereological procedures used in geology and geophysics, i.e. by observing the number of cross-sections in the material. Several such measures

have been proposed in the articles by Pietruszczak and co-workers (1989, 2003). It is noted that, the quantification of structural anisotropy in materials with a distinct microstructure (geological and biological media), was also discussed in a series of papers by Kanatani (1984, 1985).

Finally, it should also be noted that experimental/numerical studies that involve micromechanics are very useful in terms of providing an understanding of the underlying mechanisms that lead to the complex behavior at the macroscale. In the past few decades, various experimental (photo-elasticity, Dantu 1968; stereo-photogrammetry, Butterfield et al. 1970; x-rays, Roscoe et al. 1963; computed tomography, Desrues et al. 1996) as well as numerical (Discrete Element Method, Cundall and Strack 1979) research tools were developed. These tools are well suited for describing and to some extent, explaining key aspects of the behavior of granular materials, which include induced anisotropy (Oda 1972; Calvetti et al. 1997); strain localization (Bardet and Proubet 1991); influence of particle shape (Rothenburg and Bathurst 1992) and particle rotation (Oda et al. 1985). A brief review is provided by Calvetti (2003).

1.2. Scope and objectives of the present research

Granular media are very common in nature. Their mechanical behavior tends to be quite complex due to the microstructure of particle arrangement and sedimentation process. The sedimentation results in a clear horizontal stratification of the deposited

layers. The existing evidence indicates that a parallel alignment of particles is often observed in river, beach and dune sand (e.g. Oda and Koishikawa 1977) as well as artificially deposited sand (Azami et al. 2010, Symes et al. 1984). Anisotropy is clearly reflected the soil fabric composition in relation to the spatial arrangement of soil particles and voids (inherent anisotropy) and it may undergo an evolution induced by applied loads (induced anisotropy). Anisotropy in granular materials affects both the deformation response and the conditions at failure (Lam and Tatsuoka 1988, Yamada and Ishihara 1979). Consequently, it has a significant impact on the behavior of geotechnical structures (such as tunnels and foundations, slopes, retaining walls, etc.) and should be adequately accounted for in the context of design and/or stability analysis.

The objective of this work is to introduce a methodology, with experimental and analytical components, for characterizing the mechanical response of granular materials that display anisotropy. This includes conducting an experimental investigation, developing an inelastic constitutive model to describe the behavior of the material, and conducting numerical simulations on the evolution of microstructure.

This thesis consists of two major parts. Chapter 2 describes the experimental program designed to investigate the mechanical properties of sand with inherent anisotropy that is generated by initial densification process. The results of a series of direct shear tests as well as conventional triaxial tests are presented. This information provides the necessary input data for numerical analysis and forms a benchmark against

which numerical results are validated. Thereafter, the mathematical formulation is presented for describing anisotropic mechanical behavior of the material (Ottawa standard sand C109). The procedure for identification of parameters embedded in the constitutive model is outlined and the simulation results are verified against the experimental observation.

The primary focus of Chapter 3 is on developing an evolution law for the fabric of particulate materials as a function of continuing deformation. The methodology involves performing a series of Discrete Element simulations for a granular assembly under evolving directions of the principal stress/strain and defining a correlation with the evolution of material axes. It is demonstrated that granular materials with spherical particles may become anisotropic due to the initial compaction process and that the induced anisotropy is characterized by the coaxiality between the microstructure and the total strain tensors. Numerical simulations of mechanical response of granular materials with induced anisotropy are carried out by extending the framework described in previous chapter to capture the effects of induced anisotropy.

Finally, the last chapter concludes and summarizes the results of this work. In addition, some recommendations for further work are provided.

CHAPTER 2. INHERENT ANISOTROPY

2.1. Introduction

As mentioned earlier, granular materials often display anisotropy in mechanical behavior, which is strongly linked with their microstructural arrangement. Such anisotropy may occur in sands that comprise flat, elongated grains (Azami et al. 2010), but may also be induced by densification process in sands that have nearly spherical particles (Haruyama, 1981). In either case, mechanical characteristics at the macroscale display a pronounced directional dependence. This chapter is focused on examining the anisotropic response of Ottawa standard sand C109. Both experimental and theoretical aspects are addressed.

2.2. Experimental program

The inherent anisotropy in sands is known to occur if the grains are flat or elongated. The primary objective of the experimental program carried out here is to demonstrate that anisotropy may also occur in sands that have nearly spherical particles (i.e. are typically considered as isotropic) provided the distribution of pore space has a preferred orientation due to the initial densification process.

In this investigation, a series of direct shear as well as conventional triaxial tests were conducted on samples prepared at different orientations relative to the direction of deposition. The standard soil used throughout the test program was Ottawa sand C109. This is a commonly used quartz sand composed of rounded to sub-rounded particles passing the #16 sieve ($1.18mm$) and retained on the #200 sieve ($0.075mm$). Figs.1 and 2 provide the particle size distribution curve and the image of particles shape of Ottawa sand. The physical properties of the material are summarized in Table 1. In this table, the following soil index properties are given: D_{10} - grain diameter at 10% finer; D_{50} - mean grain diameter; ρ_s - density of solids; $e_{\max}$ - maximum void ratio; $e_{\min}$ - minimum void ratio; C_u - coefficient of uniformity; C_c - coefficient of curvature.

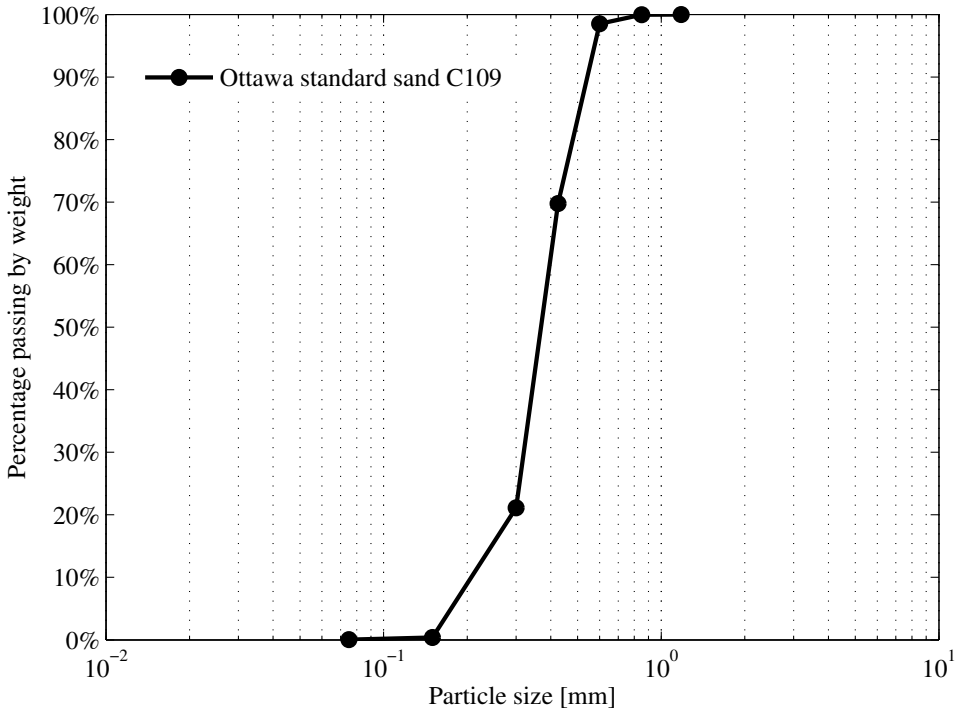

Fig. 1. Particle size distribution of ASTM graded Ottawa sand (C109)

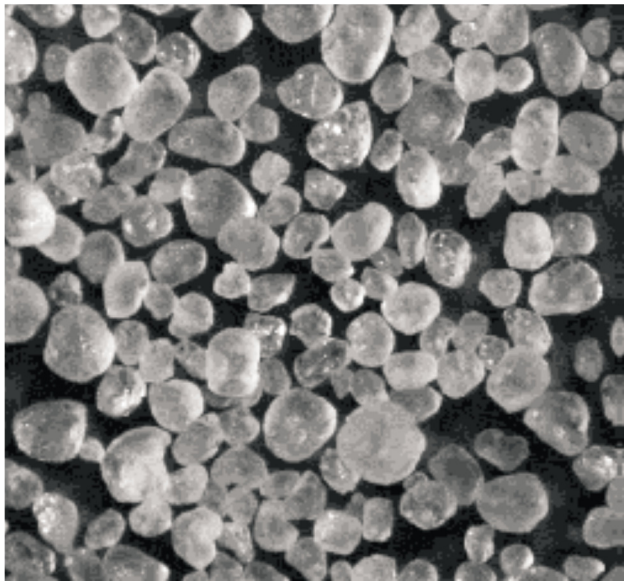

Fig. 2. Image of ASTM graded Ottawa sand (C109)
(Source: http://www.nrcresearchpress.com/doi/pdf/10.1139/t00-031)

Soil name	Quartz (%)	Feldspar (%)	Magnetite (%)	Grain type	D_{10} (mm)	D_{50} (mm)	ρ_s $(kg.m^{-3})$
C109	99.7	0	0	Sub-rounded	0.22	0.374	2648
	e_{min}	e_{max}	c_u	c_c			
	0.503	0.811	1.82	1.19			

Table 1. Ottawa standard sand: Typical physical characteristics

2.2.1. Direct shear tests

In order to investigate the directional dependency of shear strength parameters, a series of direct shear tests was conducted. The main features of direct shear apparatus are described below, along with details of sample preparation and interpretation of direct shear test data. Later, the results of the tests are presented and discussed in details.

i. Direct shear apparatus

The direct shear apparatus has been extensively described in basic soil mechanics books (e.g. Bardet 1997). The device consists of a $60\times60\times40mm$ box split in the middle in order to allow relative movement between the two halves. The normal load is applied by a rigid rough top plate and a hanger with weights. The shear load is provided by a motor which pushes the upper half of the box at a constant rate of displacement. Vertical displacement at the top boundary and shear displacements are measured by dial gauges. Shear loads are measured by a calibrated proving ring equipped with a dial gauge.

ii. Sample preparation method

The main stages of the sample preparation are summarized schematically in Fig. 3. In order to prepare samples with different orientation of material axes, a modified version of the shear box was used, as shown in Fig.4. The modification included direct shear box is obtained by cutting off one side of the standard direct shear box and making this side removable (Guo 2008).

The first stage of sample preparation involved mounting a container on a shaking table and then placing the modified direct shear box at the desired orientation, inside this container. The samples were prepared using the technique of raining which involves pluviating the sand through a grid into the container. The height of fall of sand particles during pluviation process was $500mm$ with respect to the top of the container. The sand grains were slowly poured until the container was full. It was then covered with a lid and a dead load of $2kg$ was applied at the top. The set up was then vibrated to produce specimens of desired initial void ratio. The specimens were vibrated with the amplitude of $5.3mm$ (peak-to-peak) at $5Hz$ for 40 minutes. After vibration, the extra material was carefully removed, the sample was trimmed and the removable side parts were reassembled.

The deposition angle α, is defined here as the angle between the sand rain direction and the direction normal to the plane of isotropy as shown if Fig. 3b. The deposition angles were taken as $\alpha = 0^{\circ}, 15^{\circ}, 30^{\circ}, 45^{\circ}, 60^{\circ}, 90^{\circ}$.

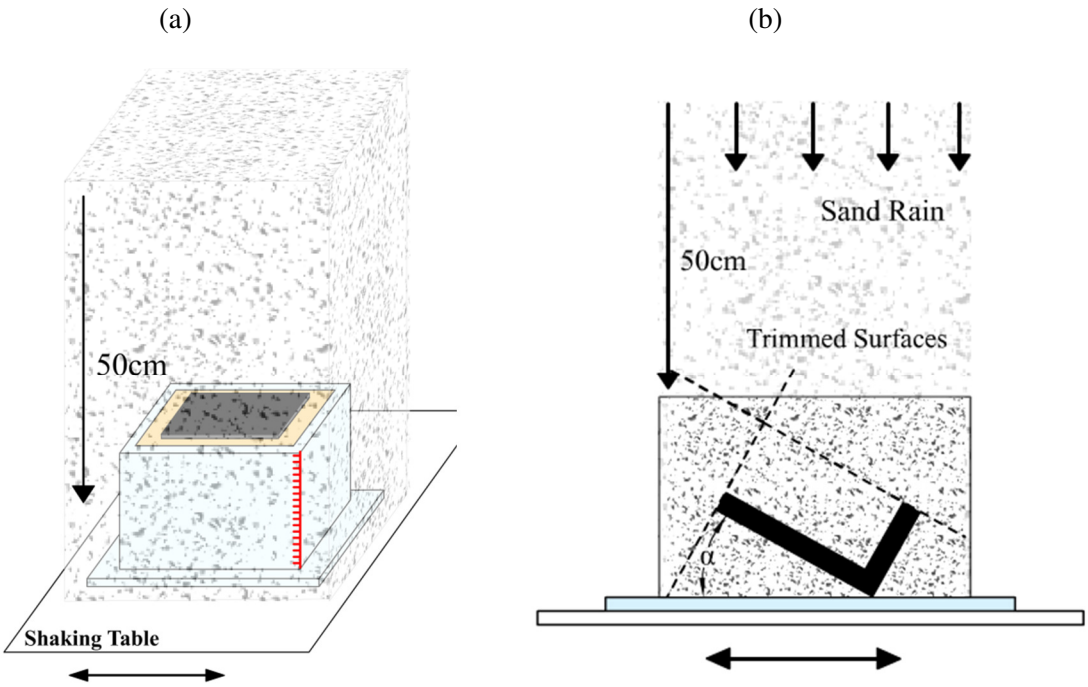

Fig. 3. Schematic diagram of sample preparation; (a) Sand pluviation; (b) Definition of angle α

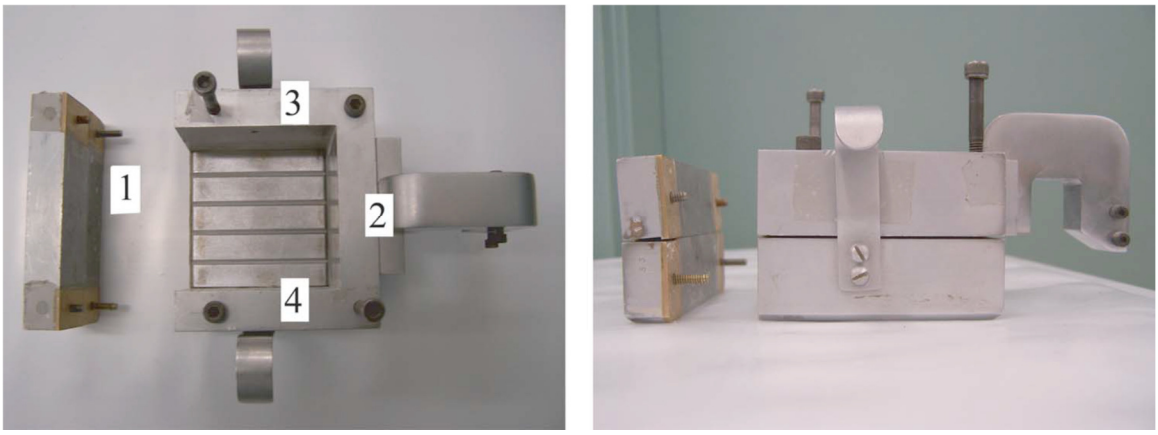

Figure 4. Modified direct shear box (Guo, 2008)

iii. Observations and interpretation of direct shear test data

The experimental measurements made during a direct shear test comprise four principal quantities, all of which are required for a proper analysis of the test, i.e.

- the shear load which is applied to the box in the horizontal direction and is transferred to the soil by the rigid end boundaries of the apparatus
- the relative shear displacement, measured in the horizontal direction, between the two halves of the shear box.
- the vertical load acting perpendicular to the central plane of shear box; this force comprises the dead load associated with the shear box apparatus and the applied load.
- and finally, the vertical displacement of the sample caused by contraction or dilation of the soil.

The interpretation of the direct shear test is based on Coulomb's notion of defining the critical combination of the shear stress τ, and normal stress σ_n, at which the failure occurs. The results of direct shear tests under different normal stresses are used to identify the classical shear strength parameters, i.e. internal friction angle ϕ and cohesion c. Usually a number of tests is conducted in order to obtain a better statistical representation

iv. Direct shear test results

The direct shear tests were performed on dry samples, with a constant displacement rate of $0.2mm/\min$, at three different levels of normal stress $\sigma_n = 10, 50, 75kPa$. The initial void ratio of all specimens was approx. 0.52. Each individual test was repeated at least once under the same testing conditions. For all tests a high degree of repeatability was observed.

The variation of shear strength and the corresponding evolution of volume change are presented in Figs. 5, 6 and 7. Clearly, in spite of nearly spherical shape of particles, the material exhibits a significant degree of anisotropy, as both the strength and deformation characteristics are affected by the angle of deposition.

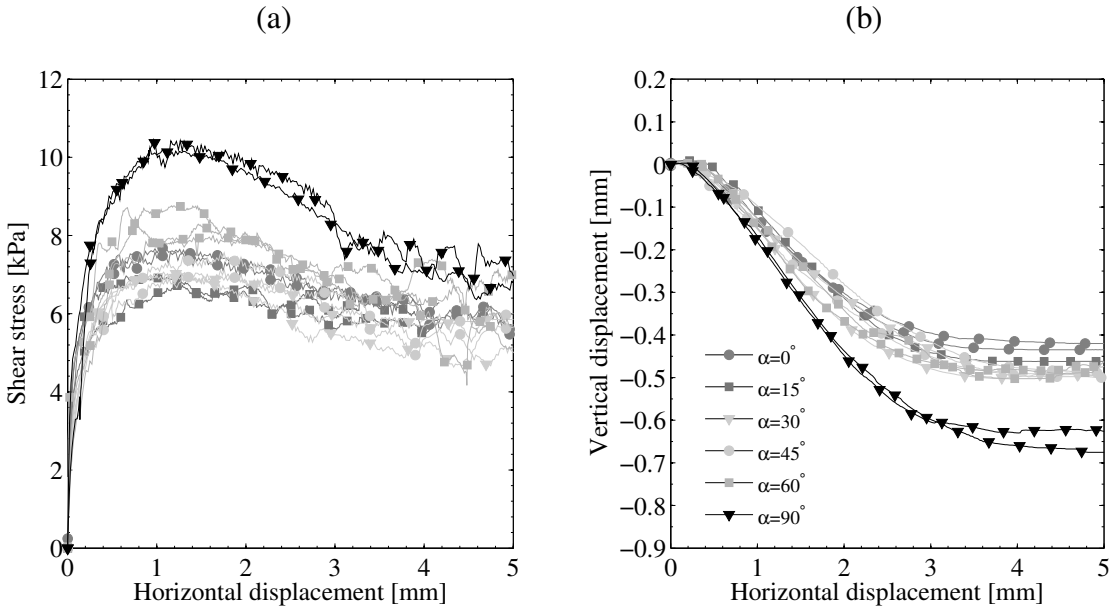

Fig. 5. Mechanical response at normal stress of $\sigma_n = 10kPa$ for different values α ; (a) Shear stress vs. Horizontal displacement characteristics and (b) Evolution of volume change.

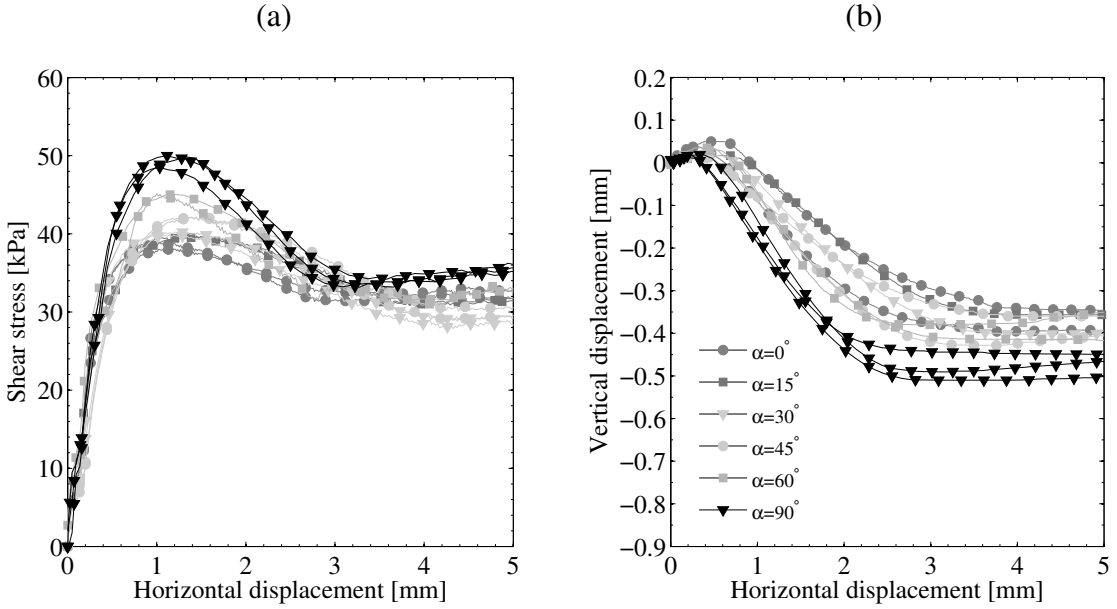

Fig. 6. Mechanical response at normal stress of $\sigma_n = 50kPa$ for different values of α ; (a) Shear stress vs. Horizontal displacement characteristics and (b) Evolution of volume change.

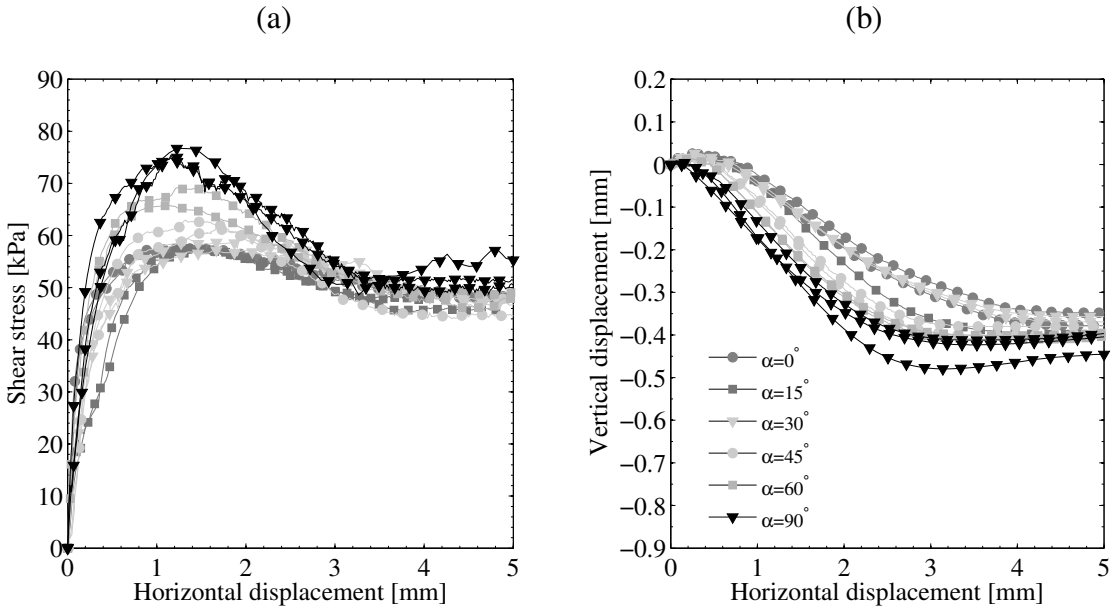

Fig. 7. Mechanical response at normal stress of $\sigma_n = 75kPa$ for different values of α ; (a) Shear stress vs. Horizontal displacement characteristics and (b) Evolution of volume change.

For all tests, the material response becomes unstable (strain softening) after reaching the peak. In terms of evolution of volume change, a progressive transition from compaction to dilatancy takes place as the shear stress increases. The dilatancy progressively increases with the increase in deposition angle α .

The failure envelopes, corresponding to linear form of Coulomb criterion are presented in Fig. 8 for different values of α . It is evident that the value of cohesion c , for Ottawa sand is negligible. Fig. 9 shows the distribution of friction angle ϕ, as a function of deposition angle α . The maximum friction angle $\phi \approx 45^{\circ}$ corresponds to shearing in

the direction normal to the plane of material isotropy. The minimum value $\phi \approx 37^{\circ}$ occurs at $\alpha \approx 15^{\circ}$.

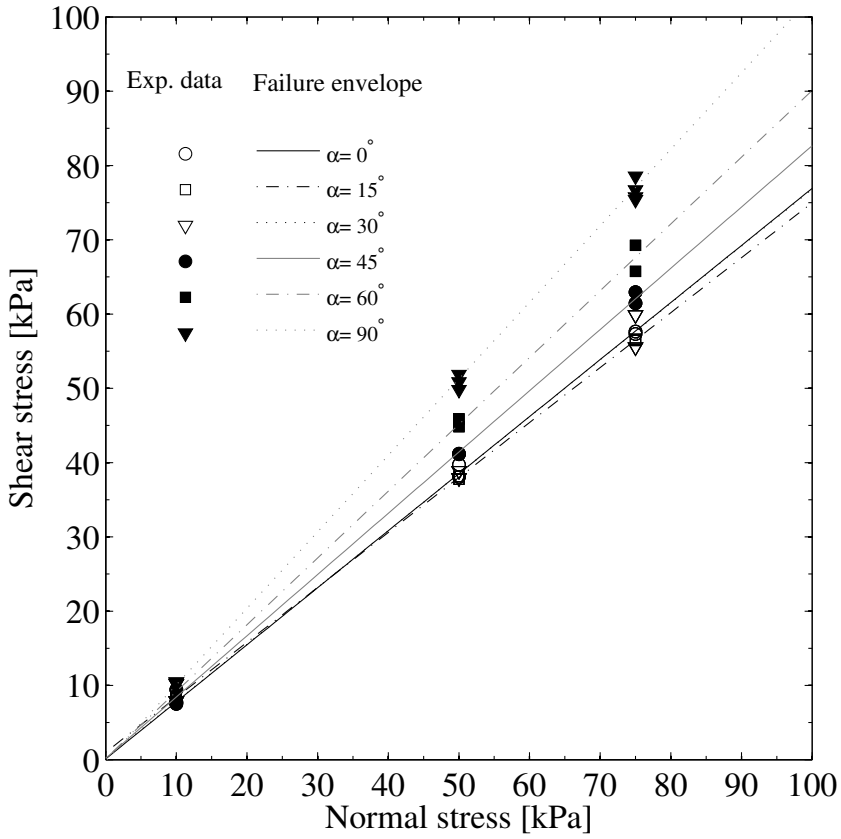

$\tau = 0.768\,\sigma_n + 0.111$	$\alpha = 0^{\circ}$
$\tau = 0.739\,\sigma_n + 1.01$	$\alpha = 15^{\circ}$
$\tau = 0.766\,\sigma_n + 0.198$	$\alpha = 30^{\circ}$
$\tau = 0.824\,\sigma_n + 0.194$	$\alpha = 45^{\circ}$
$\tau = 0.899\,\sigma_n + 0.185$	$\alpha = 60^{\circ}$
$\tau = 1.028\,\sigma_n + 0.0213$	$\alpha = 90^{\circ}$

Fig. 8. Coulomb failure envelopes for different values of α

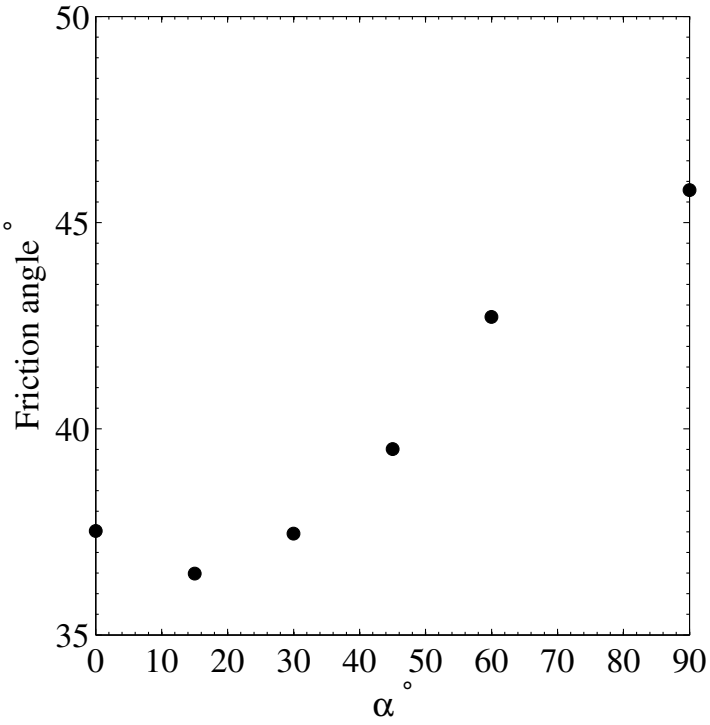

Fig. 9. Variation of friction angle ϕ with α .

Note that the results of direct shear tests will be used later to identify the material parameters for the constitutive model proposed.

2.2.2. Triaxial compression tests

A series of drained triaxial compression tests were conducted on sand samples prepared at two different orientations of material axes (i.e. $\alpha = 0^{\circ}, 90^{\circ}$). It is noted again that in triaxial test configuration, for intermediate values of α the sample has tendency to

distort under the increasing axial load. Such distortion is constrained by the presence of loading platens. Consequently, the stress field is no longer uniform and the results do not reflect the behavior of the material. Therefore, the triaxial tests were conducted on horizontal and vertical samples only.

The main features of triaxial test apparatus are described below, along with details of testing procedure and sample preparation. Later, the results of triaxial compression tests are presented.

i. Triaxial test apparatus

In a conventional triaxial test, a cylindrical specimen is enclosed in a rubber membrane and is placed in a triaxial compression chamber. The specimen is subjected to a confining fluid pressure, and then loaded axially to failure. Connections at the ends of the specimen permit controlled drainage of porewater from the specimen.

There are 3 basic types of triaxial compression tests, depending on the drainage conditions at the consolidation and shearing phases. Unconsolidated-undrained (UU) or quick (Q) triaxial test performed with the drainage valve closed for all phases of the test. In consolidated-undrained (CU) triaxial tests drainage is allowed to take place during the application of the confining pressure, but not during the shearing phase. The excess pore pressures which develop during the shearing phase are then monitored. Consolidated-drained (CD) test, also called slow test (S), is performed with free drainage condition for the whole period of the test, so that there is no generation of excess pore pressure. This

may require a slow rate in application of load. During the test, in addition to axial deformation, the volume change of the sample is monitored.

ii. Triaxial testing procedure

The triaxial testing procedure implemented in this research generally followed the standard protocol. The drained triaxial test incorporated three main stages:

- The saturation stage which involved the initial flushing of the sample with CO_2 for 15 minutes, after which the sample was flushed with de-aired water for 30 minutes. The B-test was then performed and the Skempton's B parameter, which measures the increase in pore pressure due to an increase in confining pressure, was determined. For all samples $B-$values of at least 95% were achieved.
- Isotropic consolidation which commenced subsequent to the completion of a satisfactory $B-$test. Free drainage was allowed and the volume change transducer was used to measure the void ratio change as the consolidation proceeded.
- Finally, the sample was brought to failure by applying an axial force to the loading piston of the triaxial cell. The test was run at a constant strain rate of $0.1mm/\min$.

iii. Sample preparation

The samples were prepared in a $100 \times 50 \times 50 mm$ rectangular prism mold. Analogous to the direct shear samples, the triaxial samples were prepared by the sand rain method using a constant falling height of $500 mm$. The sample was then vibrated for 5 minutes to produce specimens of desired void ratio. In this case, the amplitude and frequency of the vibration were $0.3 mm$ and $30 Hz$, respectively. The sample preparation method is illustrated in Fig. 10. It is noted that the shaking table used in this case was different from the one which is used for preparing the direct shear test samples. In both cases though the value of initial strain measured in samples due to densification process was of the same magnitude.

In order to preserve the composition of the fabric, the specimen with the mold was first submerged in water. Then, excess water was drained out under gravity to obtain a moist specimen with low moisture content. The entire setup was then frozen in order to remove the mold. The frozen specimen was subsequently transferred to the base of the triaxial cell and covered with rubber membrane. A small confining pressure was then applied while unfreezing the specimen. Finally the specimen was saturated and consolidated under a hydrostatic pressure prior to the shearing phase. To minimize the end friction effects two layers of membrane with silicon grease in between were placed between the sample and loading platens. Proper cuts were made on the membranes to allow both seepage through the sample and free lateral expansion of the sample.

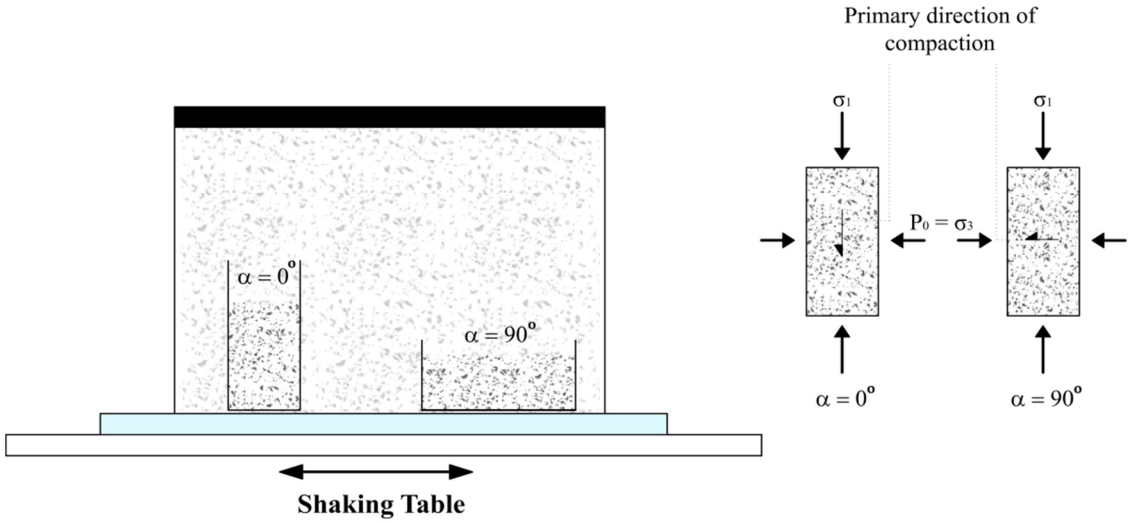

Fig. 10. Schematic diagram of sample preparation and loading configuration for triaxial tests.

iv. Triaxial test results

The results of drained triaxial tests, including the deviatoric and volumetric characteristics at initial confinement of $50kPa$ and $100kPa$, are presented in Figs. 11 and 12. The results correspond to vertical and horizontal samples. Note that at least two duplicate tests were performed in each case. It is clear that the testing procedure and the sample preparation method gave results that are very consistent and repeatable.

Figs. 11a and 12a show the strength characteristics of Ottawa sand at various confining pressures and orientations of material axes. In general, the samples tested at

$\alpha = 0$ display larger initial shear stiffness and a much higher strength. It is evident that an increase in initial confining pressure results in higher shear strength of the material.

Figs. 11b and 12b present the evolution of volumetric strain with increasing axial deformation. It is evident that the material undergoes initial compaction followed by dilation. The volume changes experienced by Ottawa sand are also influenced by confining pressure. As the cell pressure increases, the rate of dilation progressively decreases.

Based on the experimental results obtained, it may be concluded that the stress-strain behavior of dense sand strongly depends on the loading direction. Although the material tested here, i.e. Ottawa sand has nearly rounded particles, a marked inherent anisotropy is observed, which stems from a bias in the distribution of void space generated through the sample preparation procedure.

Note that the results reported here will be used later to verify the performance of the mathematical formulation. In general, basic trends in the behavior under triaxial conditions are consistent with those recorded in direct shear tests.

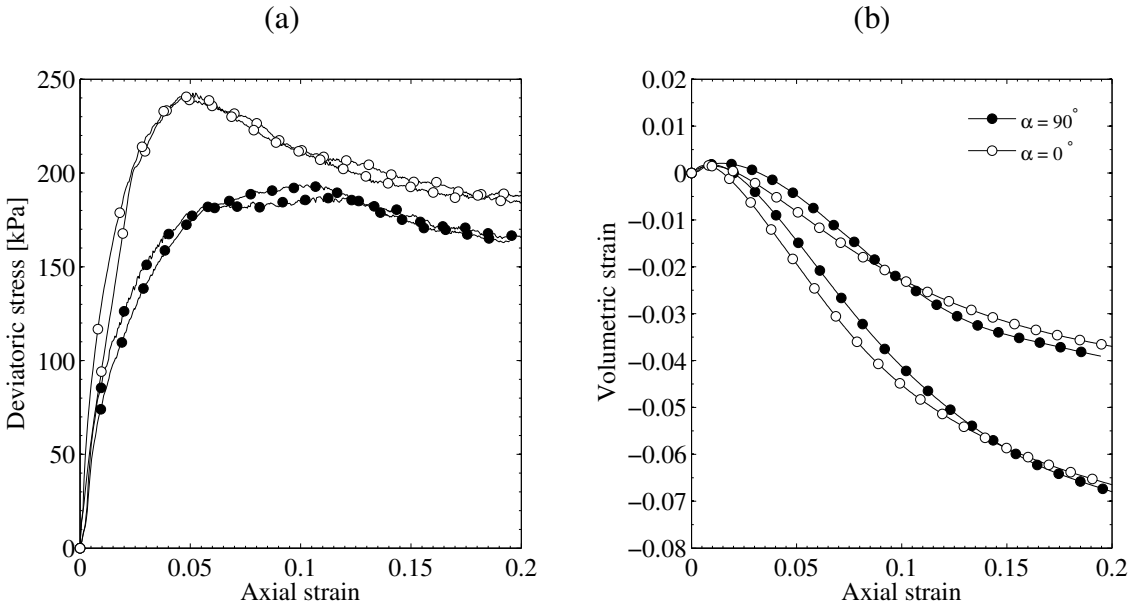

Fig. 11. Results of triaxial tests at confining pressure $P_0 = 50kPa$; variation of (a) deviatoric stress, $\sigma_1 - \sigma_3$ and (b) volumetric strain with axial strain

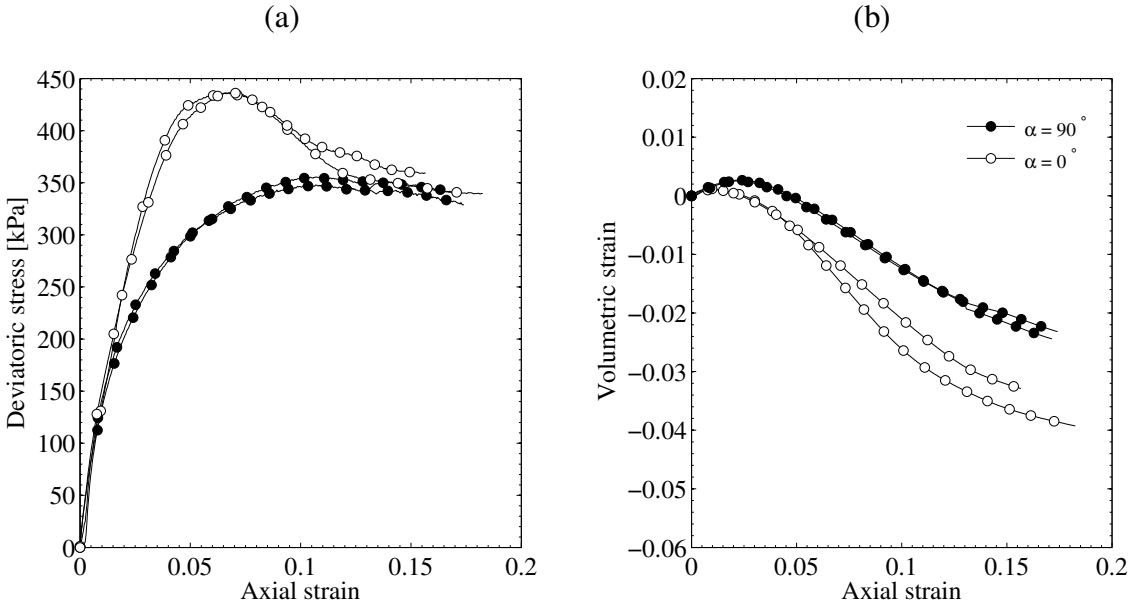

Fig. 12. Results of triaxial tests at confining pressure $P_0 = 100kPa$; variation of (a) deviatoric stress, $\sigma_1 - \sigma_3$ and (b) volumetric strain with axial strain

2.3. Mathematical formulation

2.3.1. Introduction

This section describes the mathematical formulation of the constitutive model. The specification of anisotropic failure criteria is described first, followed by the description of the deformation process. Subsequently, the procedure for specification of constants that are embedded in the constitutive relation is outlined. This procedure employs direct shear test results for identification of parameters defining both the conditions at failure and the deformation response. Later, the results of numerical simulations are presented and verified against the experimental data for triaxial compression tests at different confining pressures and sample orientations.

2.3.2. Formulation of anisotropic failure criteria (Critical Plane Approach)

The description of mechanical response of inherently anisotropic materials requires the specification of conditions at failure under an arbitrary stress state. Over the last few decades, numerous failure criteria have been proposed. One of the classical approaches to formulate the failure criteria is to invoke linear as well as quadratic terms in stress components referred to the coordinate system associated with the axes of

symmetry of the material. An example of such an approach is an extension of the well-known Hill's criterion (1950), as proposed in by Tsai and Wu (1971). An alternative approach is the one which makes use of the general representation theorems and employs ten independent basic and mixed invariants of stress and microstructure tensors (Boehler and Sawczuk 1970 and 1977). The other group of failure criteria was derived by adopting the critical plane approach. This approach requires the failure condition to be satisfied either on a predefined discrete weakness plane or on a potential failure plane corresponding to a maximum of the failure function. Examples of this approach can be found in the works by Walsh and Brace (1964), Hoek and Brown (1980), Hoek 1983. The main issue with implementation of the approaches based on general representation in terms of invariants of stress/ microstructure tensors is the fact that they require a large number of material functions/parameters to be identified. Furthermore, the correlation of these parameters with the material microstructure is rather ambiguous. Given these difficulties, simplified approaches have been introduced by Pietruszczak and Mroz (2001). The first approach to formulate the failure criteria employs a spatial distribution of strength parameters and defines the failure condition in terms of traction components acting on the critical plane. The second approach incorporates a scalar anisotropy parameter defined in terms of mixed invariants of stress and microstructure tensors. This parameter is a homogeneous function of stress of degree zero, so that it depends only on the relative orientation of the principal stress triad with respect to the eigenvectors of the microstructure tensor.

In this research the first approach proposed by Pietruszczak and Mroz 2001, is applied. In this approach, the failure criterion is defined in terms of traction components acting on the critical/localization plane. The approach employs a spatial distribution of strength parameters and the direction of the critical plane is obtained by solving a constrained optimization problem that involves searching for an orientation that maximizes the value of the failure function.

The conditions at failure are specified in terms of shear and normal components of the traction vector t_i acting on a plane with unit normal n_i , i.e.

$$\tau = \left|\sigma_{ij} n_i s_j\right| \; ; \sigma = \sigma_{ij} n_i n_j \tag{2.1}$$

$$s_i = \frac{t_i^s}{\|t_i^s\|}; \; t_i^s = \left(\delta_{ij} - n_i n_j\right)\sigma_{jk} n_k \tag{2.2}$$

For the case of Coulomb's criterion, a linear form is adopted:

$$F = \tau - \eta_f \sigma - c; \eta_f = \eta_f(n_i), \, c = c(n_i) \tag{2.3}$$

where the strength parameters are assumed to be orientation-dependent

$$\begin{aligned} \eta_f &= \eta_0(1 + \Omega_{ij} n_i n_j + a_1(\Omega_{ij} n_i n_j)^2 + a_2(\Omega_{ij} n_i n_j)^3 + \cdots) \\ c &= c_0(1 + \Omega_{ij}^c n_i n_j + b_1(\Omega_{ij}^c n_i n_j)^2 + b_2(\Omega_{ij}^c n_i n_j)^3 + \cdots) \end{aligned} \tag{2.4}$$

In the expression above, Ω's represent a set of symmetric traceless tensors which describe the bias in the spatial distribution of η_f and c. The orientation of the critical

plane can be determined by maximizing the failure function F with respect to n_i, s_i subject to the constraints; $n_i n_i = 1$, $s_i s_i = 1$ and $n_i s_i = 0$.

$$\underbrace{max}_{n_i, s_i} (F) = 0 \tag{2.5}$$

The problem can be solved using Lagrange multipliers or any other optimization technique.

2.3.3. Description of inelastic deformation

Within the critical plane framework, the inelastic deformation is attributed to sliding/separation along an infinite set of randomly orientated planes. For each plane, the conditions at failure are represented by the local criterion (2.3), which incorporates the distribution functions (2.4). The inelastic deformation is then accounted for by invoking an appropriate plasticity framework. This approach is conceptually similar to the so-called multi-laminate framework (Pande and Sharma 1983). Below, the formulation of the problems is outlined following the general framework provided by Pietruszczak and Guo (2012).

The yield/loading surfaces f, as well as the plastic potential ψ, both are defined in terms of the normal and tangential components of the traction vector acting on a plane with unit normal n_i.

$$f(n_i) = f(\sigma, \tau, \kappa) = 0 \qquad (2.6)$$
$$\psi(n_i) = \psi(\sigma, \tau) = const$$

where κ is a hardening parameter, which is a function of the plastic deformation history. The equation of the loading surface is formulated in such a manner that $\kappa \to \infty \Rightarrow f \to F$, where F is the respective failure function. Adopting a local frame of reference $\bar{x}_i$, with corresponding base vectors n_i and s_i, the flow rule is formulated as

$$\dot{\bar{g}}_i^p = \dot{\lambda} \frac{\partial \psi}{\partial \bar{t}_i} \qquad (2.7)$$

where $\dot{\bar{g}}_i^p$ is the velocity discontinuity vector and the components of the traction vector $\bar{t}_i$ are $\{\sigma, \tau, 0\}$. In order to define the strain rates contributed by this plane, a symmetric part of a dyadic product is used

$$\dot{\epsilon}_{ij}^p = \frac{1}{2t}\left(\dot{g}_i^p n_j + \dot{g}_j^p n_i\right); \qquad \dot{g}_i^p = T_{ij} \dot{\bar{g}}_j^p \qquad (2.8)$$

In the above expression, t denotes the thickness of the shear band that is associated with sliding/separation along a specific plane and T_{ij} is the standard transformation matrix which is a function of direction cosines (l_i, m_i, n_i) of the unit normal to the ith contact plane.

The average macroscopic deformation is obtained by integrating the contributions from all active planes, so that

$$\dot{\varepsilon}_{ij}^{p} = \frac{1}{8\pi t}\int_{S} \dot{\lambda}\left(T_{ip}n_j + T_{jp}n_i\right)\frac{\partial \psi}{\partial \bar{t}_p}\, dS \tag{2.9}$$

The integration is carried out over a surface area S of a unit sphere. In practical implementation, the integration process is performed numerically by adopting a set of *sampling planes* (See Fig. 13). The orientations of the sampling planes for symmetric 2×33-plane integration rule are provided in Table 2. In this table, l_i, m_i and n_i represents the direction cosines of the normal to the ith sampling plane and ω_i is the corresponding weight coefficient.

The global constitutive relation can be obtained by invoking the postulate of additivity of elastic and plastic strain rates, i.e.

$$\dot{\varepsilon}_{ij} = C_{ijkl}^{e}\dot{\sigma}_{kl} + \dot{\varepsilon}_{ij}^{p} = C_{ijkl}^{e}\dot{\sigma}_{kl} + \frac{1}{8\pi t}\int_{S} \dot{\lambda}\left(T_{ip}n_j + T_{jp}n_i\right)\frac{\partial \psi}{\partial \bar{t}_p}\, dS \tag{2.10}$$

where C_{ijkl}^{e} is the elastic compliance operator. The elastic properties associated with each sampling plane can be defined by invoking, once again, the dyadic decomposition in equation (2.8), so that

$$\dot{\varepsilon}_{ij}^{e} = \frac{1}{2t}\left(\dot{g}_i^e n_j + \dot{g}_j^e n_i\right);\ \dot{g}_i^e = T_{ij}\dot{\bar{g}}_j^e;\ \dot{\bar{g}}_i^e = k_{ij}\dot{\bar{t}}_j \tag{2.11}$$

where k_{ij} is the elastic operator follows

$$k_{ij} = \begin{bmatrix} k_N & 0 & 0 \\ 0 & k_T & 0 \\ 0 & 0 & k_T \end{bmatrix} \tag{2.12}$$

in which k_N and k_T are the normal and tangential elastic moduli of the interface, respectively, and are defined as

$$\begin{aligned} k_N &= \frac{(1-\upsilon)E}{(1+\upsilon)(1-\upsilon)t} \\ k_T &= \frac{E}{2(1+\upsilon)t} \end{aligned} \tag{2.13}$$

where E and ν are the elastic parameters of the interface material.

By rearranging the set of equations (2.11), the elastic strain rates can be defined as

$$\dot{\varepsilon}_{ij}^{e} = \frac{1}{2t}\left(T_{ip}n_j + T_{jp}n_i\right)k_{pq}T_{kq}n_l\dot{\sigma}_{kl} \tag{2.14}$$

so that the macroscopic deformation is governed by

$$\dot{\varepsilon}_{ij}^{e} = C_{ijkl}^{e}\dot{\sigma}_{kl}\ ;\ C_{ijkl}^{e} = \frac{1}{8\pi t}\int_S \left(T_{ip}n_j + T_{jp}n_i\right)k_{pq}T_{kq}n_l dS \tag{2.15}$$

In the plasticity formulation employed here, parameter κ, which is designated as the hardening parameter, is assumed to be a function of irreversible shear deformation and the loading function is defined as

$$f(n_i) = \tau - \eta\sigma - c = 0; \eta = \eta(\kappa) = \eta_f \frac{\kappa}{A+\kappa}; \kappa = \int |dg^p| \tag{2.16}$$

In the expression above, the functions $\eta_f = \eta_f(n_i)$, $c = c(n_i)$ can be approximated using the representation (2.4). Moreover, $dg^p = ((d\overline{g}_2^p)^2 + (d\overline{g}_3^p)^2)^{1/2}$ and A is a material constant. For $\kappa \to \infty$ there is $\eta \to \eta_f$ which implies that $f(n_i) \to F(n_i)$. Thus, the conditions at failure are consistent with those specified by equation (2.5).

The plastic deformation can be described by invoking a non-associated flow rule, equation (2.7), in which the plastic potential is defined as

$$\psi(n_i) = \tau - \eta_c(\sigma + \sigma_0) ln \frac{\sigma_0+\sigma}{\overline{\sigma}} = 0; \quad \sigma_0 = \frac{c}{\eta_f} \tag{2.17}$$

where $\overline{\sigma}$ is evaluated from the condition of $\psi(n_i) = 0$, where $\eta_c \sim \eta_f$ is a parameter which represents the value of $\eta = \tau - c/\sigma$ at which a transition from compaction to dilatancy takes place.

Equations (2.16) and (2.17), represent the conditions of sliding, opening/closing on the ith contact plane. The yield function for the macroscopic behavior can then be expressed as

$$f = f(n_1) \cap f(n_2) \cap f(n_3) \dots f(n_\infty) = 0 \tag{2.18}$$

where $\cap$ symbolically represents intersection of sets. Equations (2.18) represent a piecewise description of the yield function which is well established in the theory of plasticity.

Note that, within the framework described above, the evolution of yield loci is traced individually for each plane, and is a function of effective normal stress, shear stress, and plastic strains on that plane. Since the components of the traction vector depend not only on the magnitude of principal stresses but also on their directions, this framework can describe the anisotropy induced by plastic flow.

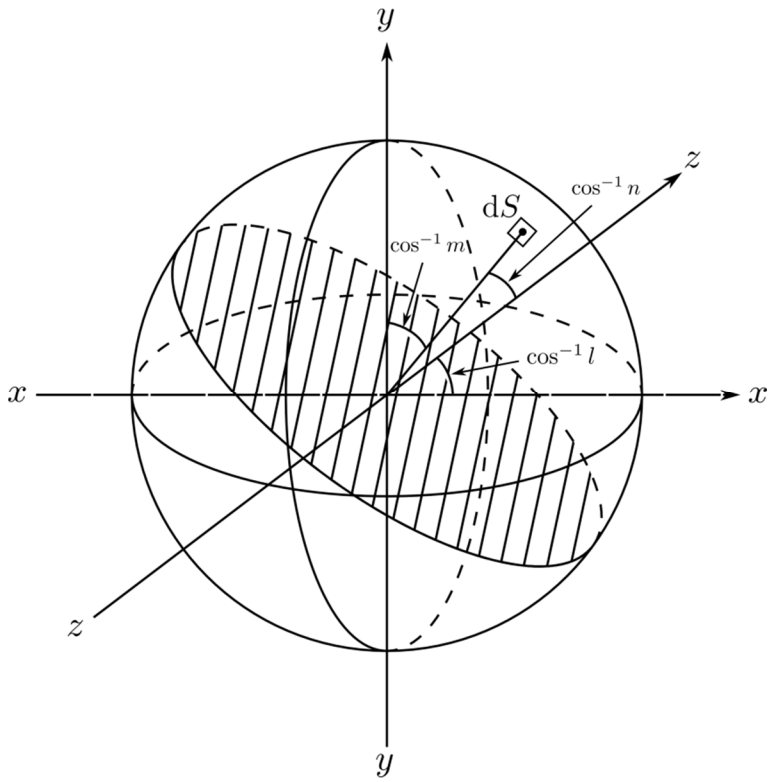

Fig. 13. Schematic diagram of infinite number of planes on the surface of a unit sphere.

i	l_i	n_i	m_i	ω_i
1	1	0	0	0.00985353993
2	0	1	0	0.00985353993
3	0	0	1	0.00985353993
4	0.7071067811	0.7071067811	0	0.01629696858
5	0.7071067811	-0.7071067811	0	0.01629696858
6	0.7071067811	0	0.7071067811	0.01629696858
7	0.7071067811	0	-0.7071067811	0.01629696858
8	0	0.7071067811	0.7071067811	0.01629696858
9	0	0.7071067811	-0.7071067811	0.01629696858
10	0.9338989563	0.3575370459	0	0.01347888440
11	0.9338989563	-0.3575370459	0	0.01347888440
12	0.3575370459	0.9338989563	0	0.01347888440
13	0.3575370459	-0.9338989563	0	0.01347888440
14	0.9338989563	0	0.3575370459	0.01347888440
15	0.9338989563	0	-0.3575370459	0.01347888440
16	0.3575370459	0	0.9338989563	0.01347888440
17	0.3575370459	0	-0.9338989563	0.01347888440
18	0	0.9338989563	0.3575370459	0.01347888440
19	0	0.9338989563	-0.3575370459	0.01347888440
20	0	0.3575370459	0.9338989563	0.01347888440
21	0	0.3575370459	-0.9338989563	0.01347888440
22	0.4372636760	0.4372636760	0.7858759158	0.01757591298
23	0.4372636760	0.4372636760	-0.7858759158	0.01757591298
24	0.4372636760	-0.4372636760	0.7858759158	0.01757591298
25	0.4372636760	-0.4372636760	-0.7858759158	0.01757591298
26	0.4372636760	0.7858759158	0.4372636760	0.01757591298
27	0.4372636760	0.7858759158	-0.4372636760	0.01757591298
28	0.4372636760	-0.7858759158	0.4372636760	0.01757591298
29	0.4372636760	-0.7858759158	-0.437263676	0.01757591298
30	0.7858759158	0.4372636760	0.4372636760	0.01757591298
31	0.7858759158	0.4372636760	-0.4372636760	0.01757591298
32	0.7858759158	-0.4372636760	0.4372636760	0.01757591298
33	0.7858759158	-0.4372636760	-0.4372636760	0.01757591298

Table 2. Direction cosines l_i, m_i and n_i weighting factors w_i of the integration planes for the symmetric 2×33 – plane integration rule (Bazant and Oh 1986)

2.3.4. Identification of material parameters

In what follows, the details of identification procedure are given for the evaluation of material parameters/functions embedded in the constitutive framework. The procedure deals with the specification of the strength parameters, the hardening constant A and the parameter η_c.

Strength parameters: The distribution of strength parameters can be directly defined based on the results of direct shear tests as shown in Fig. 8. Given these results, consider the representation (2.3), which defines the spatial variation of the parameter η_f. In order to identify this function, choose the coordinated systems as depicted in Fig. 14. Here, $\{x, y, z\}$ is the global frame of reference, while the base vectors $e_i^{(1)}, e_i^{(2)}$ and $e_i^{(3)}$, associated with the coordinate axes $\{x_1, x_2, x_3\}$, define the principal material triad. Referring the problem to the principal material system, there is $\Omega_1 = \Omega_3$ and since Ω_{ij} is a traceless operator (i.e. $\Omega_1 + \Omega_2 + \Omega_3 = 0$), the following representation is obtained

$$\Omega_{ij} n_i n_j = \Omega_1 (1 - 3\cos^2 \alpha) \tag{2.19}$$

so that

$$\begin{aligned} \eta_f = \eta_0 (1 + \Omega_1 (1 - 3\cos^2 \alpha) + a_1 (\Omega_1 (1 - 3\cos^2 \alpha))^2 \\ + a_2 (\Omega_1 (1 - 3\cos^2 \alpha))^3 + \cdots) \end{aligned} \tag{2.20}$$

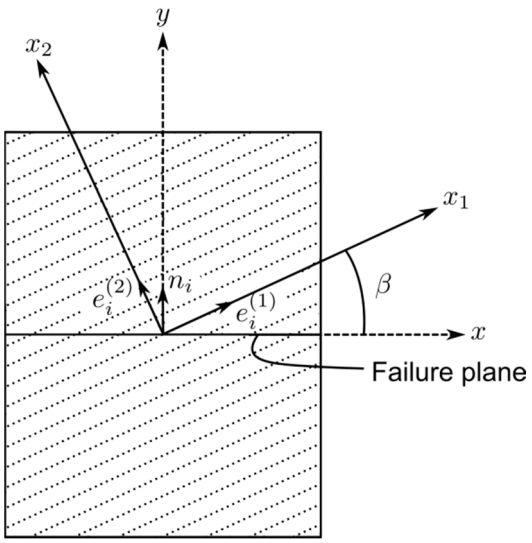

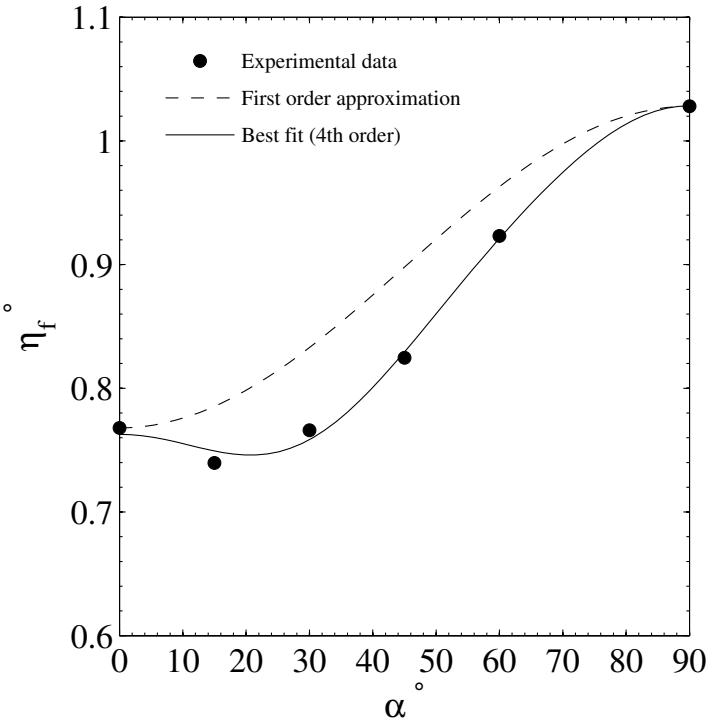

Fig. 14. Approximations to spatial variation of the friction coefficient η_f

The best fit approximations employing representation (2.20) are shown in Fig. 14. The results incorporate the dyadic products of order 1 and 4, respectively. Evidently, the approximation including terms up to order 4 is more accurate and corresponds to

$$\eta_0 = 0.8896, \Omega_1 = 0.1398, a_1 = 0.3956, a_2 = 0.4457, a_3 = 18.96 \tag{2.21}$$

Note that, since the values of cohesion c, are negligible here ($c = 0$ i.e. the material poses no resistance to tension), the anisotropy effects are attributed only to variation of η_f.

Parameter A: In order to identify the material constant A, which appears in the hardening function, equation (2.16), the mechanical characteristics given in Figs. 5, 6 and 7 were re-plotted in $\{g^p, \eta = \tau - c/\sigma\}$ space. The irreversible part of the horizontal displacement discontinuity, g^p, can be estimated via the additivity postulate. The latter requires the identification of the elastic tangential modulus $\mathrm{K_T} = d\tau/dg^e$. Note that, since, the experimental information available here, is limited to active loading histories, the value of $\mathrm{K_T}$ was estimated from the initial slope of the *loading* branch.

Fig. 15 shows the variation of $\mathrm{K_T}$ with the deposition angle, α, for different normal stresses $\sigma_n = 10, 50, 75 kPa$. It is evident that the value of $\mathrm{K_T}$ increases with an increase in normal stress magnitude; however, the orientation dependency is not very significant and can, in fact, be neglected. The orientation average of $\mathrm{K_T}$ estimated as

$K_T = 365\,kPa/mm$, was selected as representative over the range of $\sigma_n = 50, 75kPa$ and was employed in the numerical simulations.

Fig. 16 presents the hardening characteristics at normal stress σ ranging from 10 to $75kPa$, for deposition angles $\alpha = 0^\circ, 60^\circ$ and 90°. The best fit approximations employing the hyperbolic representation viz. equation (2.16), are also shown. It is evident that the experimental characteristics become unstable (strain softening) after reaching the peak. This will, in general be associated with formation of shear band and localization of deformation, when samples are tested under more general loading conditions (e.g. in triaxial or biaxial tests). The modeling of localized deformation mode should be dealt with at the level of a boundary-value problem. As this is not explicitly addressed here, the identification procedure is restricted to hardening regime, including the specification of the onset of unstable response. Note that, since the hardening function is of the type $g^p \to \infty \Rightarrow \eta \to \eta_f$, perhaps the simplest approach is to define the asymptotic condition as $g^p \to \infty \Rightarrow \eta \to \zeta\eta_f$, where ζ is a constant within the range, say $1 < \zeta < 1.05$. In such case, the onset of unstable response can be associated with $\eta = \eta_f$.

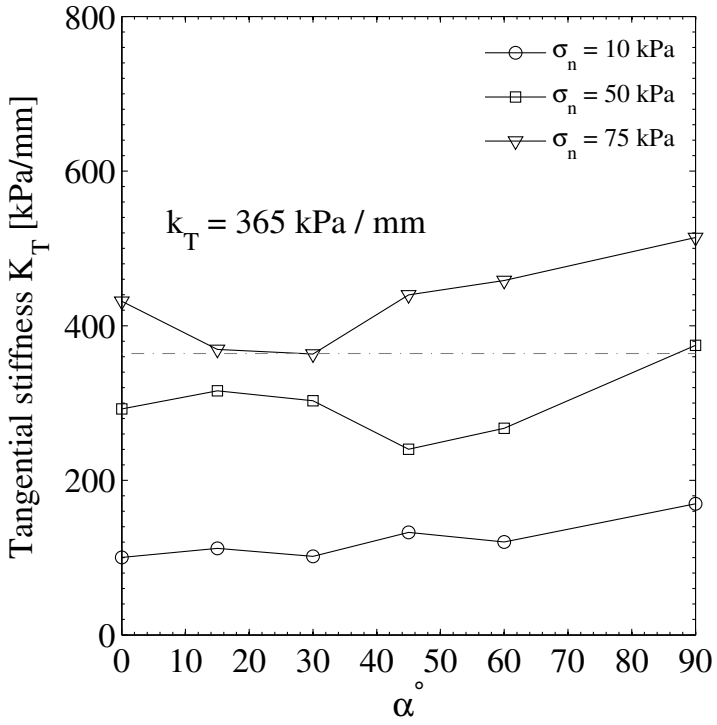

Fig. 15. Variation of K_T with angle, α

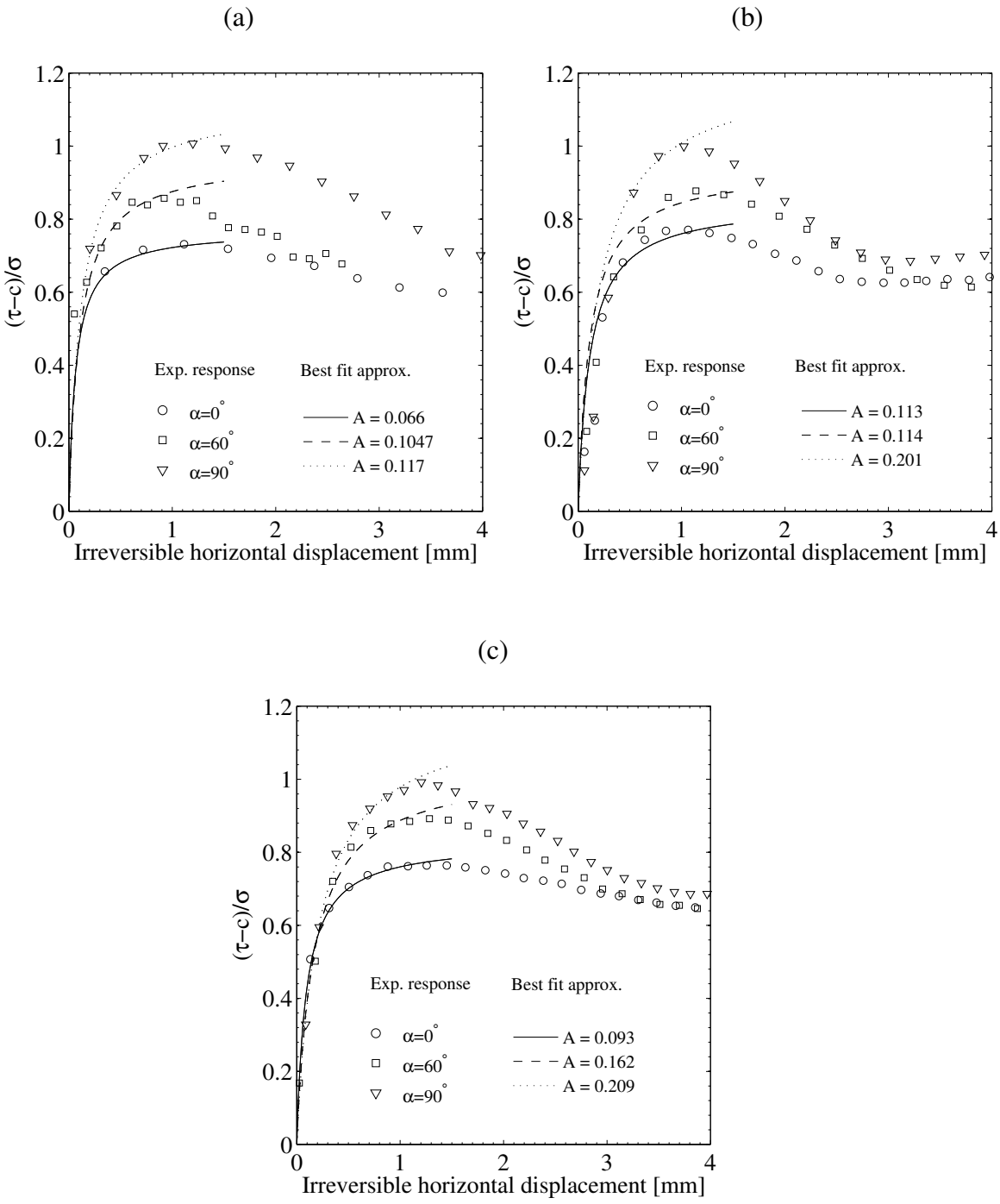

Fig. 16. Hardening characteristics of sand samples; (a); $\sigma_n = 10kPa$ (b); $\sigma_n = 50kPa$ (c) $\sigma_n = 75kPa$

Given the set of results presented in Fig. 16, the spatial variation of parameter A, can be established (See Fig. 17). In general, the orientation dependence of A is not very pronounced. Thus a constant value of $A = 0.158mm$ which is the orientation-average for tests conducted at $\sigma_n = 50kPa$ and $\sigma_n = 75kPa$, was selected as representative and was employed later in the numerical simulations.

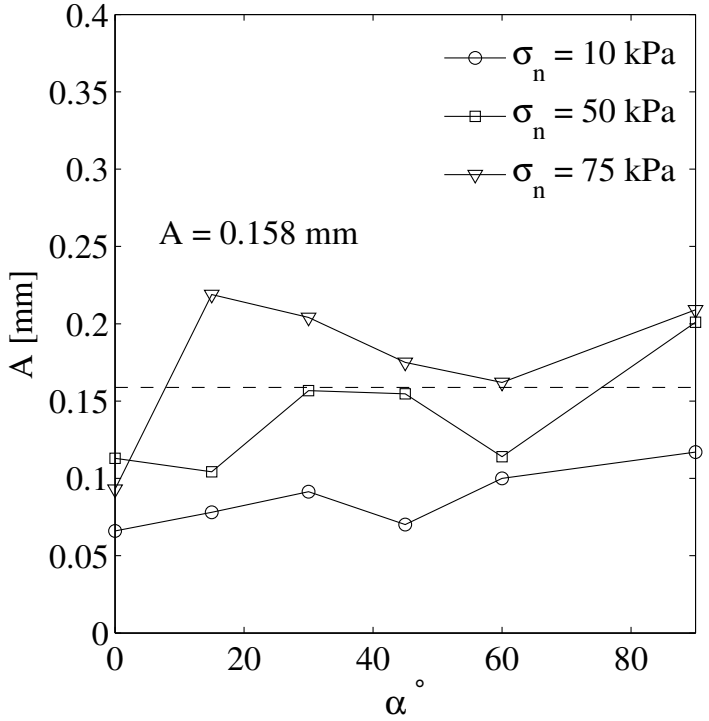

Fig. 17 Variation of hardening parameter A with angle α

Parameter η_c: The next step of identification procedure involves the specification of the plastic potential function, which requires evolution of parameter η_c. This parameter defines the transition from plastic compaction to dilatancy. The information on

the material parameter that governs this transition can be obtained from the same set of direct shear tests as before by examining the nature of deformation characteristics. Again these characteristics need to be re-plotted in the affine space $\{\eta=(\tau-c)/\sigma, g_1^p\}$. The irreversible part of the vertical displacement discontinuity, g_1^p, has been determined by assuming that $K_N=5K_T$ and invoking the additivity postulate. Note that, in general, a sufficient degree of accuracy may be maintained by estimating the transition points from the evolution of total vertical displacement discontinuity, rather than from its irreversible part. Fig. 18 shows the evolution of volume change for $\alpha=60^\circ$ at normal stress $\sigma_n=75kPa$. In this case the estimated value of η_c is approximately 0.6 which corresponds to the maxima of the volume evolution curve.

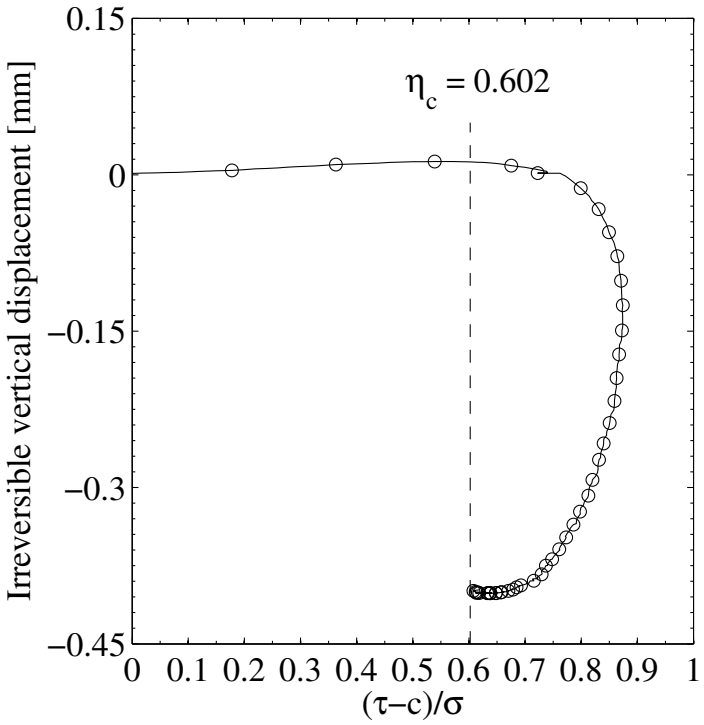

Fig. 18. Specification of the onset of dilation at $\sigma_n = 75kPa$; $\alpha = 60^\circ$

Fig. 19 shows the variations of η_c with the deposition angle α at normal stresses of $\sigma_n = 50kPa$ and $\sigma_n = 75kPa$. It is evident that the evolution of η_c is qualitatively similar to that of the strength parameter. Therefore, the estimated value of η_c was taken as $\eta_c = 0.65\eta_f$.

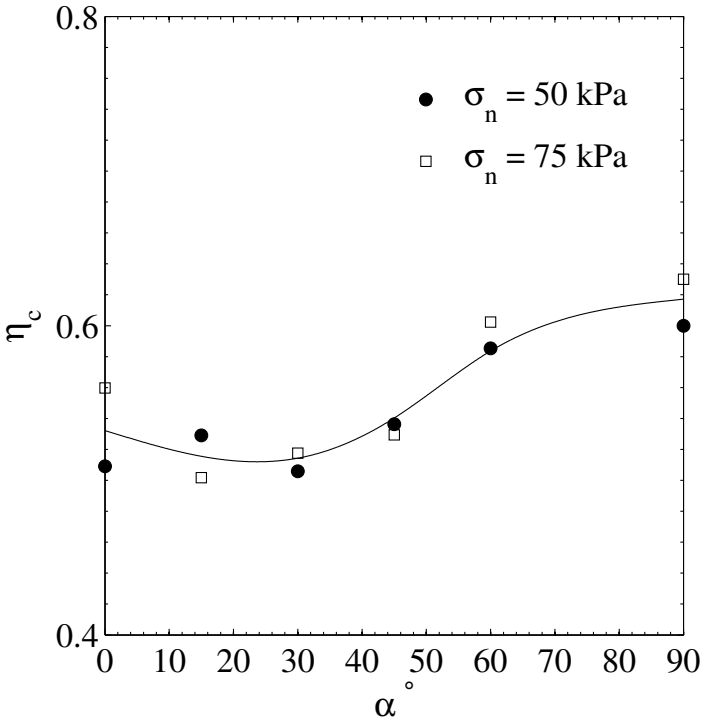

Fig. 19. Variation of with η_c angle α

Finally, the thickness associated with sliding/separation along each specific plane was assumed to be a multiple of the average particle size, viz. $t = 6mm$. Furthermore, given the evidence provided in Fig. 14 the elastic properties were taken as isotropic.

A set of material parameters that have been identified based on considerations above, is provided in Table 3.

Elastic properties	Hardening parameter	Strength parameter	Plastic potential function parameter
$\mathrm{K_T} = 365\ kPa/mm$ $t = 6\ mm$ $\upsilon = 0.33$ $E = 6MPa$	$A = 0.158\ mm$	$\eta_0 = 0.8896$ $\Omega_1 = 0.1398$ $a_1 = 0.3956$ $a_2 = 0.4457$ $a_3 = 18.96$	$\eta_c = 0.65\eta_f$

Table 3. Material parameters for simulations of mechanical response of sand samples

2.3.5. Numerical analysis of drained behavior of sand

The performance of the constitutive framework outlined in sections 2.3.2 and 2.3.3 has been verified by simulating the drained triaxial tests described in Section 2.2.2.

Figs. 20 and 21 show the results of simulations of tests conducted at initial confining pressures of $P_0 = 50kPa$ and $P_0 = 100kPa$ for the deposition angles of $\alpha = 0^\circ$ and 90°. The results include the deviatoric stress-strain characteristics, as well as the evolution of volume change. The simulations do not involve the unstable strain softening response, as the latter is associated with the onset of localized deformation and, as mentioned earlier, should be analyzed at the level of a boundary-value problem.

It should be mentioned that the deformation mode is axisymmetric only for the sample tested at $\alpha = 0^\circ$. For $\alpha = 90^\circ$ the lateral deformation is different in the respective

in-plane directions, while for samples at other orientations, the generation of shear strains will be predicted. It is evident that the obtained results, in terms of strength and volumetric characteristics, are fairly consistent with the experimental evidence. In particular, the predicted maximum level of the deviatoric stress intensities is close to the observed values. Also, the evolution of volume change shows a transition from a compaction to dilation, while the quantitative response is not very sensitive to the orientation of the sample, which is also consistent with the experimental observation.

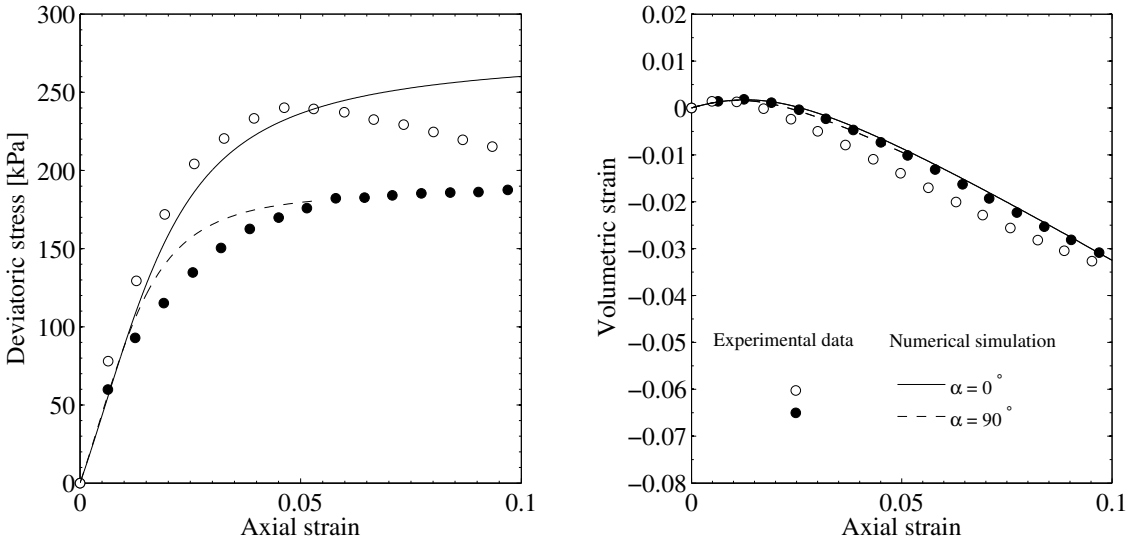

Fig. 20. Results of triaxial compression tests at $P_0 = 50kPa$; (a) stress-strain characteristics and (b) evolution of volume change (model parameters: $t = 6mm, E = 6MPa, A = 0.158mm$)

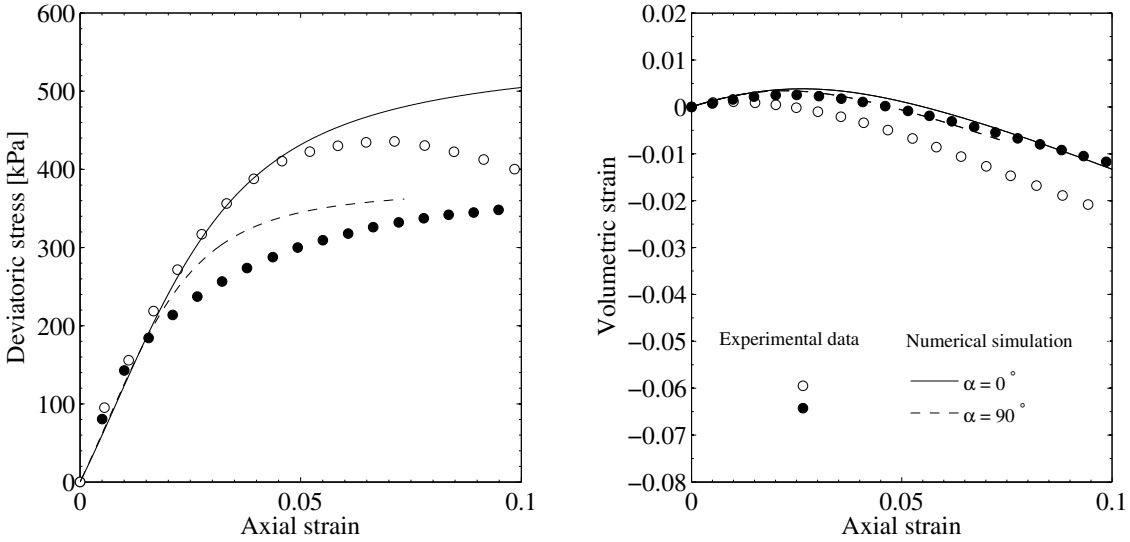

Fig. 21. Results of triaxial compression tests at $P_0 = 100kPa$; (a) stress-strain characteristics and (b) evolution of volume change (model parameters: $t = 6mm, E = 6MPa, A = 0.158mm$)

CHAPTER 3. LOAD INDUCED EVOLUTION OF FABRIC OF GRANULAR MATERIALS

3.1. Introduction

As mentioned earlier, many naturally occurring geomaterials are anisotropic at the macroscale, which is strongly related to their microstructure. In granular materials, the anisotropy may originate from the shape of the grains. It is well known, for example, that the strength properties of sand with elongated angular-shaped aggregates are strongly affected by the direction of loading in relation to the direction of deposition (Oda et al. 1978). But even if the particles are nearly spherical, the response may be anisotropic which can be attributed to a bias in the distribution of void space due to initial compaction. In this case, the anisotropy may evolve during the deformation process. Whether inherent, induced or a combination of both, the anisotropy in microstructure may have a significant effect on both the strength and deformation characteristics of the material and should be accounted for in the context of analysis and design of geotechnical structures.

Over the last few decades, an extensive research effort has been devoted to study the anisotropy effects in geomaterials. In terms of formulation of the problem, the

focus has been on specification of the conditions at failure in materials that display an inherent anisotropy. In this case, the principal material directions are defined a priori and remain constant during the deformation process. One of the classical approaches to formulate the failure criteria is to invoke linear as well as quadratic terms in stress components referred to the coordinate system associated with the axes of symmetry of the material. An example of such an approach is an extension of the well-known Hill's criterion (Hill 1950), as proposed by Tsai and Wu (1971) and Pariseau (1972). The main issue with implementation of these approaches is the fact that they require a large number of material parameters whose correlation with the material microstructure is rather ambiguous. Given these difficulties, a simplified approach has been introduced by Pietruszczak and Mroz (2001), which employs a scalar anisotropy parameter defined as a homogeneous function of stress of degree zero, so that it depends only on the relative orientation of the principal stress triad with respect to the eigenvectors of the microstructure tensor.

In certain geomaterials, in particular in granular materials, the inherent anisotropy is often weak and can easily be altered in the course of deformation process. In this case the problem is more complex, as a specific fabric descriptor needs be employed and an appropriate evolution law must be specified. The research on correlating the changes in material microstructure with the applied mechanical load has been quite limited. For particulate materials with elongated grains, the evolution of fabric at different stages of triaxial testing has been examined in recent work of Fonseca et al.

(2013). In general, however, the formulation of an appropriate evolution law is difficult. This stems primarily from difficulties associated with experimental setups providing more general loading paths e.g. rotation of principal stress axes. In addition, a continuous monitoring of the changes in structural arrangement, e.g. via computed tomography (CT) measurements, is required which is quite complex in itself. An alternative approach, which is the main focus in this work, involves formulation of the evolution law based on numerical simulations of the mechanical response of a particulate assembly and its correlation with the evolution of fabric. Such a study is conducted here using the Discrete Element Method (DEM).

It should be noted that the description of anisotropy typically entails specification of the spatial distribution of strength parameters with respect to the coordinate system associated with material axes (cf. Pietruszczak and Mroz 2001). For geomaterials with a strong *inherent* anisotropy (e.g., sedimentary rocks) the latter are defined *a priori* and remain fixed during the deformation process. In this case, the distribution of strength parameters can be assessed directly from appropriate experimental tests and no explicit measure of fabric is required. This is in contrast to the class of materials which initially have no preferred orientation but may experience an *induced* anisotropy. Here, the principal material directions change and an appropriate evolution law needs to be formulated in order to trace it. This, in turn, requires an explicit fabric descriptor and its correlation with stress/strain rates. It should be emphasized that a specific fabric measure

is, in general, needed only to monitor the evolution of the principal material axes, and it's not necessarily employed in the formulation of the constitutive relation.

In the next section, the notion of description of the microstructure of granular media is addressed and some descriptors, which are based on stereological measurements, are reviewed. Later, a series of numerical simulations are carried out examining the correlation between the external load and the evolution of microstructure. It is demonstrated that in a typical granular medium, like sand at different degrees of initial compaction, the evolution law may be formulated by imposing coaxiality between the microstructure and the total strain tensors. A comprehensive parametric study has been carried out to examine the influence of various material parameters on the general conclusion emerging from this work. The proposed evolution law is suitable for describing the effects of *induced* anisotropy in granular materials that are isotropic in terms of the grain architecture.

3.2. Description of structural anisotropy

In granular materials, the evolution of anisotropy during the deformation process stems from the rearrangement of particles and the associated change in the void space distribution. Materials experiencing deformation induced anisotropy require, in general, some measures that quantify the material fabric.

Over the last few decades several different measures of microstructure have been proposed. In this work, the focus is on descriptors that employ the basic principles of stereology. Stereology provides efficient techniques for extracting quantitative structural data from measurements made on a set of two-dimensional planar sections within the Representative Elementary Volume (REV) of the material by sampling in a statistical sense. The statistical sampling principles guarantee that no bias is introduced in choosing sections. The procedure involves the use of geometric probes, i.e. points or lines, which are superimposed on sections to measure sums and numbers of intersections with the structural feature of interest. Stereological analyses have been broadly applied in the area of bone mechanics. An example here is the concept of 'mean intercept length' (MIL) (Whitehouse 1974, Harrigan and Mann 1984), which was developed to describe the anisotropy of trabecular bone architecture. In the area of geomechanics, the concepts of 'directional porosity' (Pietruszczak and Krucinski 1989) and/or the 'areal pore size distribution' (Inglis and Pietruszczak 2003) have been developed to quantify the spatial distribution of void space within the REV. Several other stereology based fabric measures, such as the 'mean free path tensor', e.g. (Kuo et al. 1989, Oda et al. 1985), and 'damaged surface area tensor' (Wang et al. 2002) have also been introduced and identified through different imaging techniques.

Stereological measurement procedures involve both high and low order dimensional probes, such as points, lines and planes to measure various quantities of interest, including length, surface area, volume, etc. Lineal probes are particularly

appropriate for deriving orientation dependent information. In this study, fabric measures which rely on parallel arrays of lineal probes have been included. The probes are equally spaced and are rotated from a standard alignment configuration into a prescribed sampling direction.

Consider the following basic measurement quantities derived from an array of parallel test lines. Let $l(n_i)$ be the total length of test lines in the direction n_i Furthermore, let $\sum I(n_i)$ represent the sum of all intersections of these test lines with the void space, while $N(n_i)$ corresponds to the number of intercepts. The two fabric measures employed in this work are defined below (after Inglis and Pietruszczak 2003). The measurements are taken over a *REV*, which is considered in the form of a spherical domain of radius R. A Cartesian coordinate system is then fixed at the centroid of this sphere.

i. Mean intercept length (*MIL*): For a grid of uniformly distributed parallel lines aligned in the direction n_i, the *MIL* descriptor is defined as the total length of intercepts with the void space divided by the number of intercepts. Thus,

$$MIL(n_i) = \frac{\sum I(n_i)}{N(n_i)} \tag{3.1}$$

ii. Areal porosity (n): The identification process involves cutting the sphere with a plane of unit normal v_i and placing on it a set of uniformly

distributed parallel lines aligned in an arbitrary direction, ω_i (i.e., $v_i\omega_i = 0$). The fraction of voids on this plane is then evaluated as

$$\rho(v_i) = \frac{1}{2\pi}\int_{C(v_i)} g(\omega_i)\, dC\ ;\ g(\omega_i) = \frac{\sum I(\omega_i)}{l(\omega_i)} \tag{3.2}$$

where $C \subset (0, 2\pi)$ is the angle measured in this plane and $g(\omega_i)$ is symmetric with respect to the origin; i.e., $g(\omega_i) = g(-\omega_i)$. The areal porosity $n(v_i)$ is obtained by averaging ρ along the direction v_i, i.e.

$$n(v_i) = \frac{1}{2\pi}\int_{-R}^{R} \rho(v_i)\, dL \tag{3.3}$$

where dL is the differential distance measured along v_i. The integration in equation (3.3) can be replaced by a discrete summation. For this purpose, consider a set of equally spaced, parallel test lines on any set of m equally spaced, parallel planes. The test lines are rotated in-plane k times around a pole defined by v_i. Thus, in terms of the discrete quantities I and N

$$n(v_i) = \frac{1}{m}\sum_{j=1}^{m} \rho^j(v_i);\quad \rho^j(v_i) = \frac{1}{k}\sum_{k} \frac{\sum I(\omega_i^k)}{l(\omega_i^k)} \tag{3.4}$$

In order to increase the accuracy of the numerical integration, it is convenient to assume that the test line density remains constant on all m

planes. Therefore, in the case of a spherical sampling domain, the test line spacing within each planar disc perpendicular to the sampling direction is different. The closest spacing between test lines occurs on discs near the poles, whereas the farthest spacing occurs at the equatorial plane.

Given the definition of fabric measures, viz. equations (3.1) and (3.3), the mathematical representation of the spatial distribution of $MIL(n_i)$ and/or $n(v_i)$, referred to as $f(v_i)$, may be taken in the general form proposed by Kanatani (1985).

$$f(v_i) = C(1 + \Omega_{ij} v_i v_j + \Omega_{ijkl} v_i v_j v_k v_l + \cdots) \tag{3.5}$$

where Ω_{ij} describes the bias in the distribution and C represents the mean value of the respective descriptor. For a smooth orthogonal anisotropy, it is sufficient to retain the term incorporating the second rank traceless tensor Ω_{ij}, i.e. (Pietruszczak 2010)

$$f(v_i) \approx C(1 + \Omega_{ij} v_i v_j) \tag{3.6}$$

However, in order to attain a higher degree of accuracy in fitting the measurement data, the representation (3.6) can be extended by incorporating dyadic products of the second rank tensor, similar to expression (2.4) (cf. Pietruszczak and Mroz 2000 and 2001). In this case, the modified l th order approximation can be expressed as

$$f(v_i) = C\left(1 + \Omega_{ij} v_i v_j + \sum_{k=2}^{l} a_{k-2} \, (\Omega_{ij} v_i v_j)^k\right) \tag{3.7}$$

Note that the mathematical framework for describing the mechanical response does not necessarily employ explicit fabric measures like those defined by equation (3.1) or (3.3). Instead, a relation is established that specifies the spatial variation of strength/deformation parameters with respect to the coordinate system associated with the material triad (Pietruszczak and Mroz 2000). For both representations (3.6) and (3.7), the principal material directions are defined by the eigenvectors of the tensor Ω_{ij}. In the course of the deformation process, those directions may progressively change and the main focus of this work is on establishing a general form of the evolution law.

The postulate put forward here is that for granular materials with no inherent anisotropy, undergoing a continuous deformation, the principal directions of the microstructure remain collinear with the strain tensor. Thus, the evolution law can be written as

$$n_{ij}^{\Omega} = \alpha n_{ij}^{e} + \beta n_{ij}^{e} n_{ij}^{e};$$

$$n_{ij}^{\Omega} = \frac{\Omega_{ij}}{(\Omega_{kl}\Omega_{kl})^{1/2}};\ n_{ij}^{\mathrm{e}} = \frac{\mathrm{e}_{ij}}{(\mathrm{e}_{kl}\mathrm{e}_{kl})^{1/2}} \tag{3.8}$$

where e_{ij} is the strain deviator and α, β are constants. Alternatively, a linear form may be employed that corresponds to $\beta = 0$, in which case

$$n_{ij}^{\Omega} = \alpha n_{ij}^{e} \quad \vee \quad \dot{n}_{ij}^{\Omega} = \alpha \dot{n}_{ij}^{\mathrm{e}} \tag{3.9}$$

The numerical study presented in the following sections is aimed at examining the validity of this postulate.

3.3. Numerical simulations

The evolution of internal structure was investigated here by employing the Discrete Element Method (DEM). The simulations were carried out using the computer code $PFC^{2D}4.0$, from Itasca Consulting Group, Inc. (2012). Since the primary objective in this work was to establish the qualitative trends in the evolution of fabric, a simplified two-dimensional analysis was conducted. The two-dimensional analogues of particulate media have been extensively used in the past to examine the mechanical response. Examples include physical experiments using photoelastic disks e.g. Drescher and Jong (1972) as well as tests using Schneebeli rods e.g. Ibrahim et al. (2010). In the context of numerical analysis, the 2D visualization of particle displacements and contact force networks is much easier, making these analogues quite useful in studying particle-scale mechanics in detail. In addition, the two-dimensional simulations are significantly less time consuming than their 3D counterparts.

3.3.1. Numerical tests setup

The details on sample generation are presented in the Appendix A. The sample has been created by random generation of particles whose particle size follows a prescribed particle size distribution (PSD) curve. In particular, the PSD curve employed here corresponds to Ottawa sand, as discussed in Chapter 2. The load induced evolution of internal structure, has been investigated using a combined loading path. The sample was subjected to axial compression followed by a test involving a continuous rotation of principal strain axes. Fig. 22 shows the schematic diagram of imposed strain paths. The definitions of stress and strain tensors are based on the volume averaging technique outlined in Li et al. (2013).

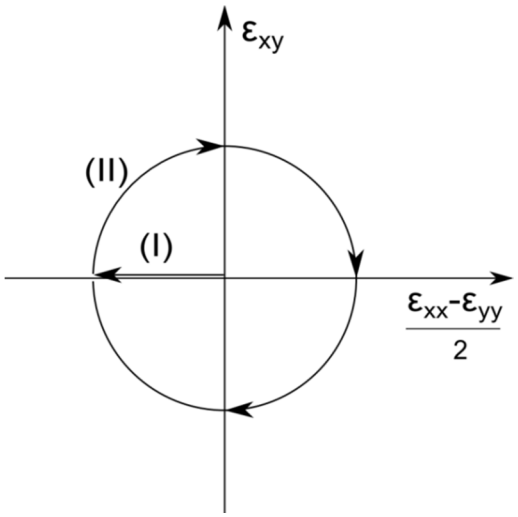

Fig. 22. Schematic diagram of strain path

During the axial compression stage, the principal axes of strain and stress are fixed. The vertical stress σ_1 is increased while the horizontal stress σ_2 is kept constant.

Two pairs of rigid boundaries impose kinematic constraints on boundary particles. The principal strain increments are applied in vertical direction while a servo-control mechanism controls the movements of horizontal boundaries in order to maintain the horizontal stress $\sigma_2 = 100kPa$ during the test. Several relaxation steps were performed within each increment in order to minimize the transient inertial effects that would have biased the results of presumed quasi-static loading.

In the next stage of loading, the sample is subjected to a pure rotation of principal strain axes at constant volumetric strain ε_v and deviatoric strain ε_q. Note that in two-dimensional case, there is $\varepsilon_v = J_1(\varepsilon_{ij})$ and $\varepsilon_q = \sqrt{J_2\left(\varepsilon_{ij}\right) - J_1^2\left(\varepsilon_{ij}\right)/4}$, so that the strain tensor ε_{ij} can be expressed as

$$\varepsilon_{ij} = \frac{\varepsilon_v}{2}\begin{pmatrix}1 & 0\\ 0 & 1\end{pmatrix} + \varepsilon_q\begin{pmatrix}sin^2\alpha_\varepsilon - cos^2\alpha_\varepsilon & -2\ \sin\alpha_\varepsilon \cos\alpha_\varepsilon\\ -2\ \sin\alpha_\varepsilon \cos\alpha_\varepsilon & cos^2\alpha_\varepsilon - sin^2\alpha_\varepsilon\end{pmatrix} \quad (3.10)$$

A strain-controlled scheme has been employed by controlling the movements of rigid boundaries. A differential change in the strain direction $\Delta\alpha_\varepsilon$ was applied, so that $\alpha_\varepsilon^{i+1} = \alpha_\varepsilon^i + \Delta\alpha_\varepsilon$. The strain increment was then calculated as $\Delta\varepsilon_{ij} = \varepsilon_{ij}^{i+1} - \varepsilon_{ij}^i$ and was applied on specimen boundaries following the procedure described in Li et al. 2013.

Figs. 23 and 24 show some typical results in terms of the evolution of deviatoric stress and volumetric strain against the increase in the deviatoric strain during the axial compression. The results correspond to an assembly of 1000 particles with contact shear

stiffness $K_S = 2\times10^5 N/m$ contact stiffness ratio $K_S / K_N = 1$ and interparticle friction angle $\phi_s = 30^\circ$. At the end of the axial compression, the incremental change in the direction of principal strain axes, $\alpha_{\Delta\varepsilon}$ was imposed. Figs. 25 and 26 show the corresponding evolution of the deviatoric strain components. It is evident that the imposed principal strain axes rotation is coupled with the rotation of principal stress axes, Fig. 27. The relation between $\alpha_{\Delta\varepsilon}$ and α_σ is shown in Fig. 28. The direction of the principal stress system, α_σ, deviates by an average of 30° from that of the principal strain increment $\alpha_{\Delta\varepsilon}$. Similar results were obtained experimentally by Matsuoka and Sakakibara (1987).

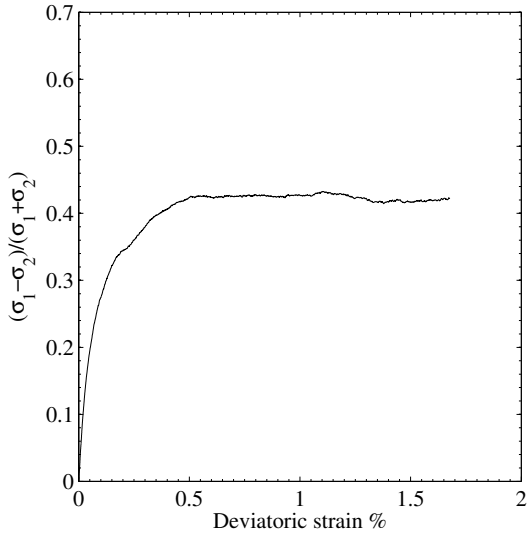

Fig. 23. Evolution of normalized deviatoric stress with deviatoric strain

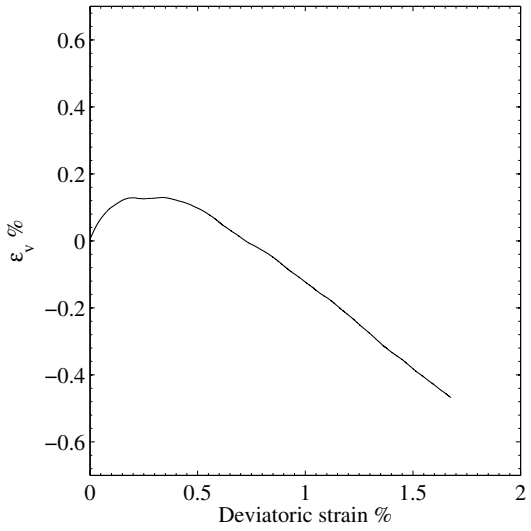

Fig. 24. Evolution of ε_v with deviatoric strain

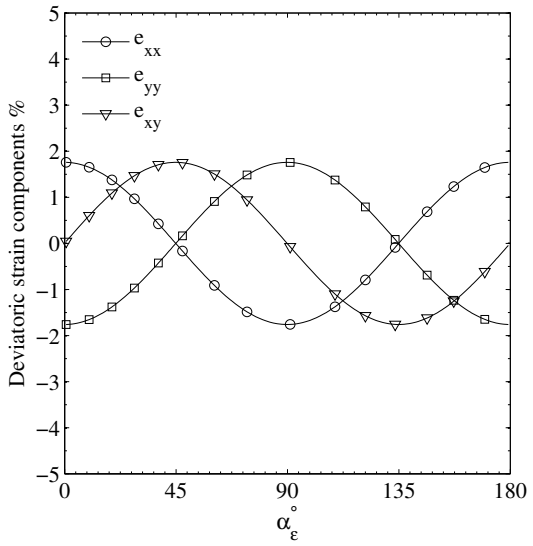

Fig. 25. Variation of the deviatoric strain components with the direction of principal strain

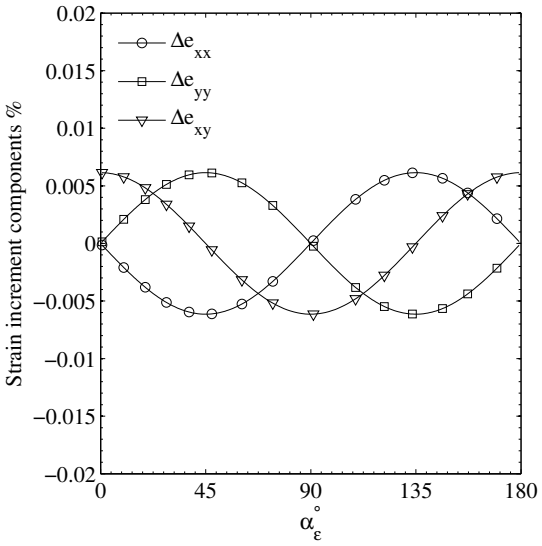

Fig. 26. Variation of the deviatoric strain increment components with the direction of principal strain

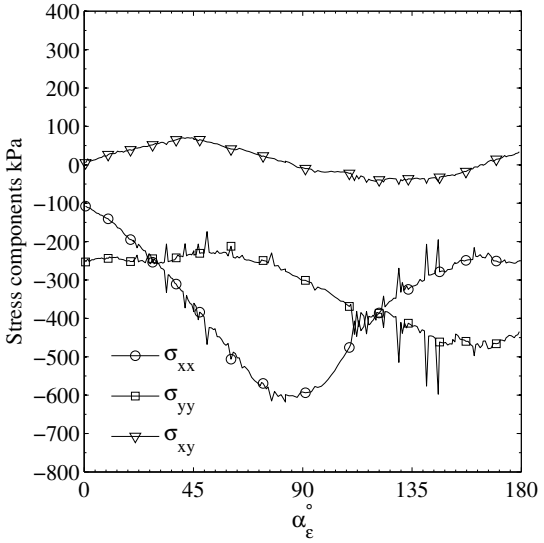

Fig. 27. Variation of stress components with the direction of principal strain

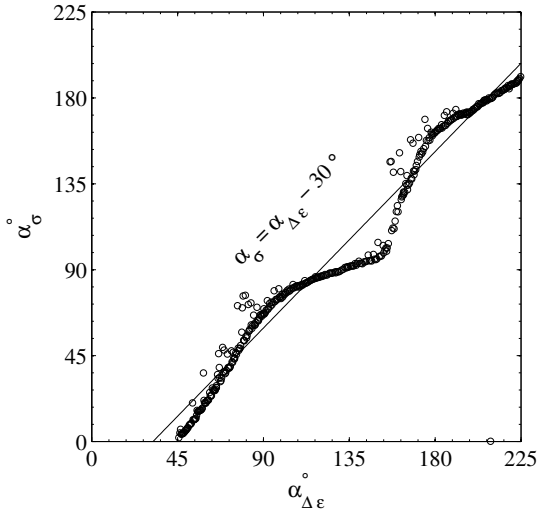

Fig. 28. Relation between α_σ and $\alpha_{\Delta\varepsilon}$

3.3.2. Parametric studies

Here, the influence of key variables including the contact shear stiffness K_S, contact stiffness ratio K_S/K_N and the interparticle friction angle ϕ_s, on the macroscopic response of the sample are examined. The selected range of model parameters is quite wide in order to enable the assessment of their influence on the macroscopic response of the sample. In addition, the influence of sample size (i.e. number of particles) is also investigated. The details of the parametric study are provided in Table 4. Here, N denotes the number of particles, H and W refer to the sample height and width, respectively, D_{50} denotes the median particle diameter and n_0 is the initial porosity.

Regarding the influence of sample size, the macroscopic response for three different samples with N equal to 2000, 4000 and 10000 is shown in Figs. 29 and 30. The results do not significantly change with an increase in the sample size. Given this conclusion, the sample size used for the evaluation of the evolution of fabric was chosen as $N = 4000$, which is a reasonable compromise between the accuracy and the calculation effort. In addition, the ratios of sample width and sample height to the median particle diameter (i.e. D_{50}) were taken as equal to 127 and 112, respectively.

Test ID	N	H [mm]	W [mm]	H/D_{50}	W/D_{50}	n_0	K_N [N/m]	K_S [N/m]	K_S/K_N	ϕ_s
N1	2000	30	30	85	85	16.1%	2×10^5	2×10^5	1	30°
N2	4000	43	43	121	121	15.7%	2×10^5	2×10^5	1	30°
N3	10000	74	74	209	209	15.8%	2×10^5	2×10^5	1	30°
T01	4000	45	40	127	112	15.4%	2×10^5	2×10^4	0.1	20°
T02	4000	45	40	127	112	15.4%	2×10^5	2×10^4	0.1	30°
T03	4000	45	40	127	112	15.4%	2×10^5	2×10^4	0.1	40°
T04	4000	45	40	127	112	15.4%	2×10^5	2×10^5	1	20°
T05	4000	45	40	127	112	15.4%	2×10^5	2×10^5	1	30°
T06	4000	45	40	127	112	15.4%	2×10^5	2×10^5	1	40°
T07	4000	45	40	127	112	15.1%	5×10^4	5×10^4	1	30°

Table 4. Details of the parametric study

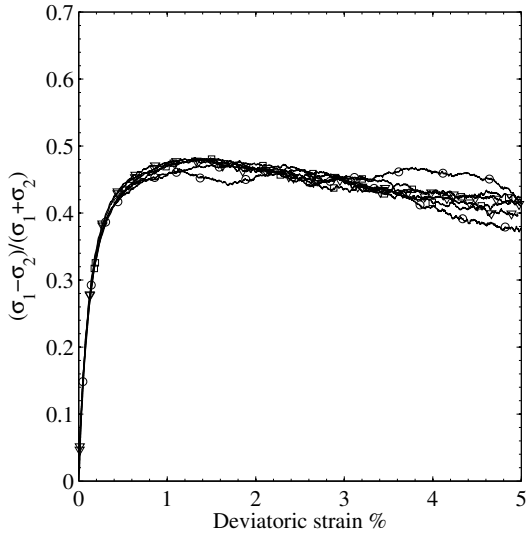

Fig. 29. Evolution of normalized deviatoric stress with deviatoric strain for different values of N

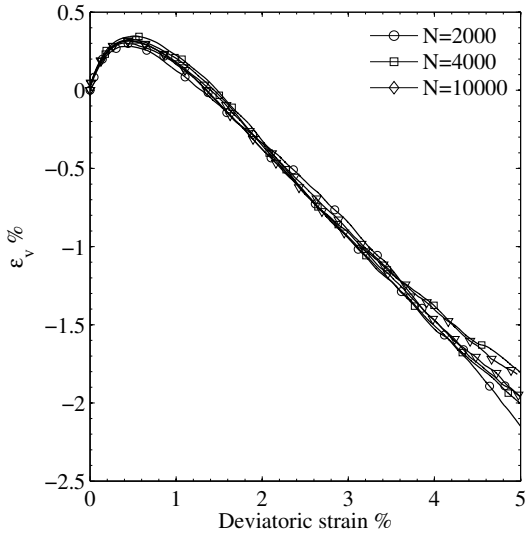

Figure 30. Evolution of volumetric strain with deviatoric strain for different values of N

A number of axial compression tests with varying interparticle friction angle ϕ_s and contact stiffness ratio K_S/K_N were carried out to investigate the influence of the

material parameters on the specimen response. The detailed information is again provided in Table 4. In each series of tests, the confining pressure was equal to $100kPa$ and the initial void ratios were approximately the same. The results of simulations are given in Figs. 31 and 32.

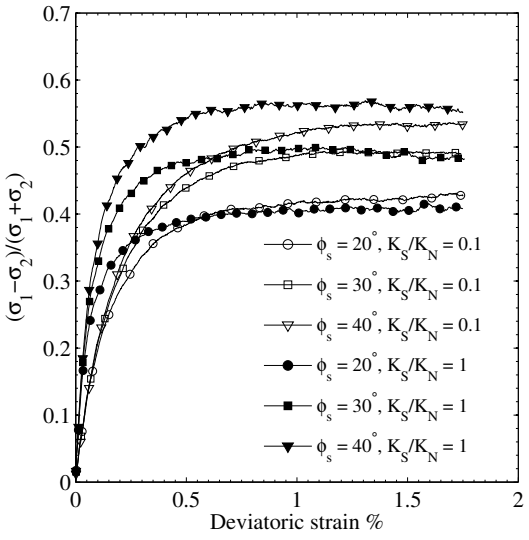

Fig. 31. Evolution of normalized deviatoric stress with deviatoric strain for different values of K_S / K_N and ϕ_s

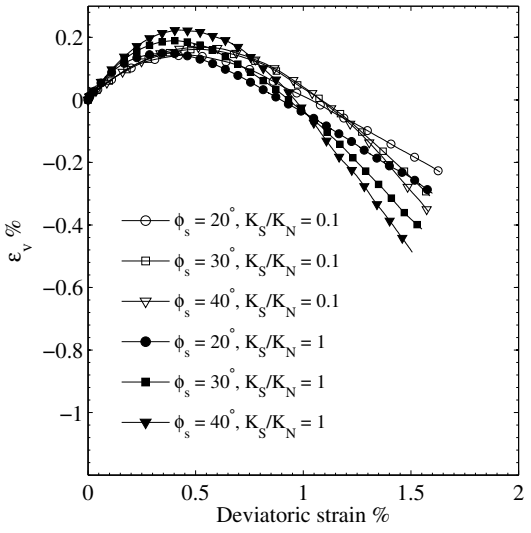

Fig. 32. Evolution of volumetric strain with deviatoric strain for different values of K_S / K_N and ϕ_s

The results show that the friction coefficient affects the strength as well as the deformation characteristics of the sample. As the friction angle increases both the ultimate stress ratio and the rate of dilatancy increase. The results corresponding to different values of K_S are shown in Figs. 33 and 34.

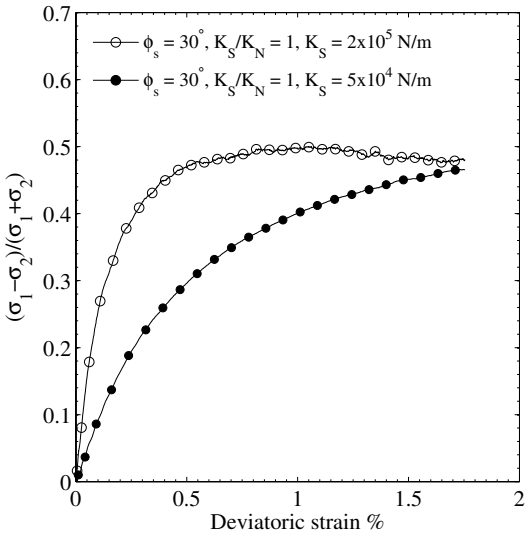

Fig. 33. Evolution of normalized deviatoric stress with deviatoric strain for different values of K_S

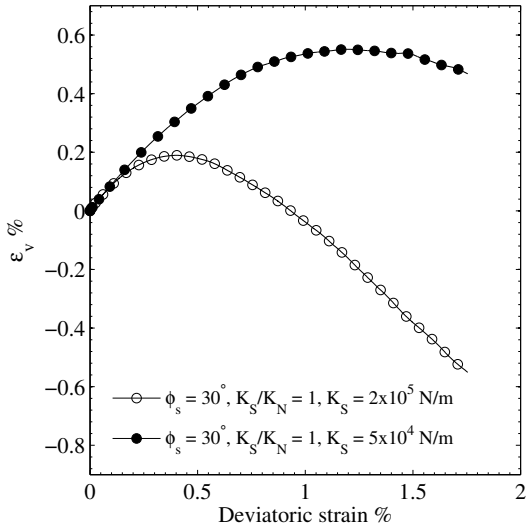

Fig. 34. Evolution of volumetric strain with deviatoric strain for different values of K_S

3.4. Evolution of fabric during the deformation process

3.4.1. Quantifications of fabric measures

The procedure for computing the three basic quantities, i.e. $l(n_i)$, $N(n_i)$ and $\sum I(n_i)$, from which fabric measures are calculated, is outlined first. The process begins with specification of the geometry of the sampling domain. To reduce the boundary effects, a circular cut through the middle of the specimen was used such that 15% of the specimen width was disregarded in the vicinity of vertical boundary segments, as depicted in Fig. 35. A set of equally spaced parallel test lines of direction θ and grid

spacing d was then placed, as shown in Fig. 36. The intercept measurements were taken for all test line segments arising from the intersection of the test lines with the sampling domain. Fabric measures were calculated from ratios of the sums of basic intercept quantities.

Note that the radius and position of all particles are available from DEM simulations. Given this information, an algorithm was developed for detecting the intersections of test lines with particles boundaries. An intercept length is defined as the distance between two points on the boundaries of two neighboring particles measured along the test line. Sums and numbers of intercept lengths were determined for each individual test line and then progressively updated.

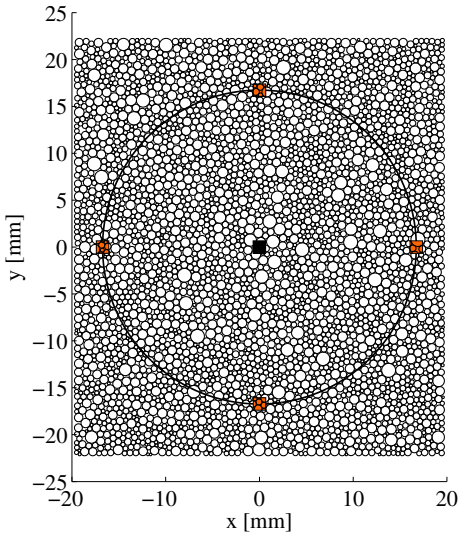

Fig. 35. 2D specimen from DEM simulation

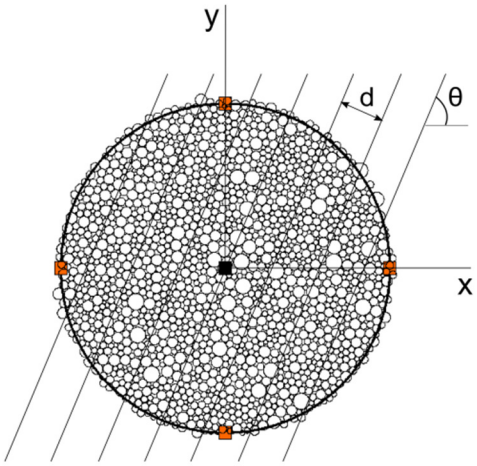

Fig. 36. A family of test lines of orientation θ and grid spacing d within the sampling domain

For the purpose of verification, the values of initial porosity obtained from DEM simulations data were reassessed for tests T06 and T07 using the procedure outlined above. The $n(v_i)$ measurements were obtained using a sampling domain of diameter $33.4\ \text{mm}$ and a grid spacing of $5\ \mu\text{m}$. The mean values of $n(v_i)$ measurements are in reasonable agreement with the values of initial porosity obtained from DEM simulations data as shown in Table 5.

Tests ID	**T06**	**T07**
Initial porosity (2D)	15.4% (DEM simulation)	15.1% (DEM simulation)
	15.3% (Measured mean porosity)	15.0% (Measured mean porosity)
Dimension of sampling domain	Diameter 33.4 mm	
Grid spacing	5 μm	

Table 5. General characteristics of sampling domain

To select suitable grid spacing, samples were subjected to a series of preliminary scans to determine the mean porosity relative percentage error over a range of grid spacings. Fig. 37 shows the results corresponding to tests T06 and T07. Based on these results, a grid spacing of 5μm was adopted. Note that in the present study the sampling directions were varied in 10° increments from $\theta = 0^{\circ}$ to 180° .

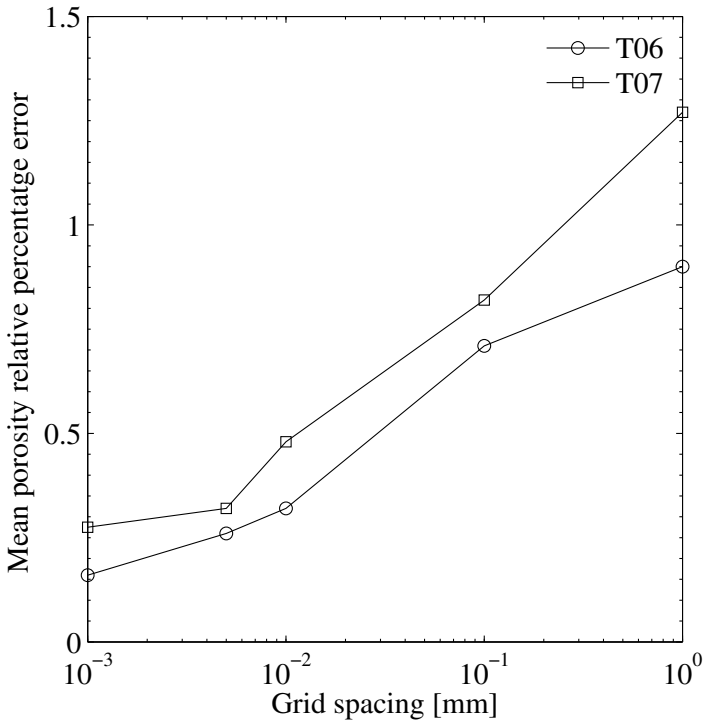

Fig. 37. Grid spacing versus mean relative percentage error in porosity for tests T06 and T07

Fig. 38 shows the distribution of 'areal porosity' n at the end of axial compression stage. The results correspond to test T06 at deviatoric strain 1.75%. The best fit approximations employing equation (3.7) are also shown. The results incorporate the dyadic products of orders 1 through 3, respectively.

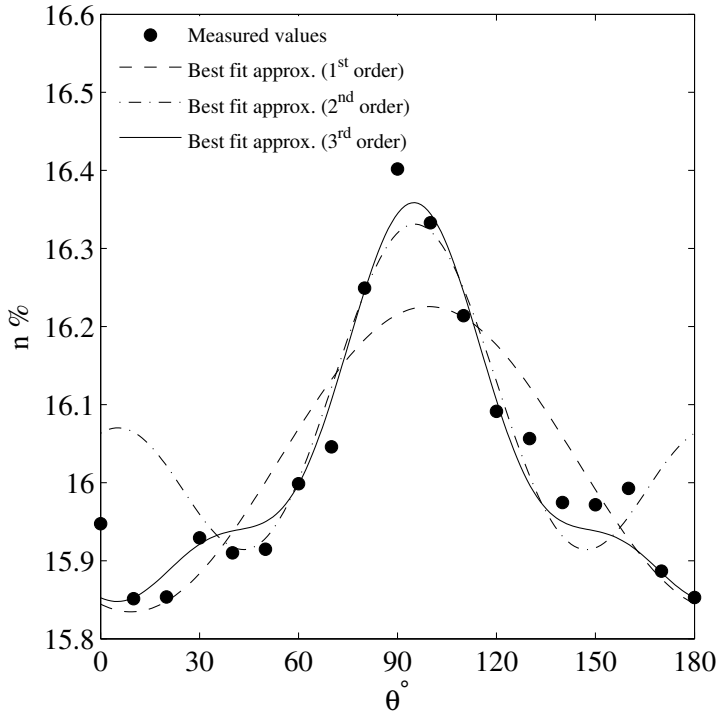

Fig. 38. Distribution of fabric measure n

3.4.2. Numerical results

During the axial compression, the principal material axes remain coaxial with those of principal strain/stress. In the DEM simulations, however, the inhomogeneity of the sample and the boundary conditions result in a small nonconformity. Let δ be the angle between the respective eigenvectors of Ω_{ij} and those of the strain deviator. Fig.39 shows the evolution of δ during axial compression obtained using the 'areal porosity' as the fabric measure. For each test examined here, the mean value and the standard deviation of the angle δ are also given. It is evident that, at the start of the axial

compression stage, a small deviation of principal material directions from principal strain directions is observed. This deviation is inherited at the particle generation stage and is compounded by the isotropic compression in which a servo-control mechanism is used to bring the assembly to the initial stress state. During the axial compression stage, a further small increase in δ takes place with a gradually decreasing rate. The mean values of δ vary from $-4.22 \mp 0.68^{\circ}$ for T06 test to $-4.62 \mp 1.02^{\circ}$ for T01 test. This threshold deviation is not considered significant here and has virtually no impact on the conclusions emerging from this work. It is noted that for all cases, almost the same response is observed.

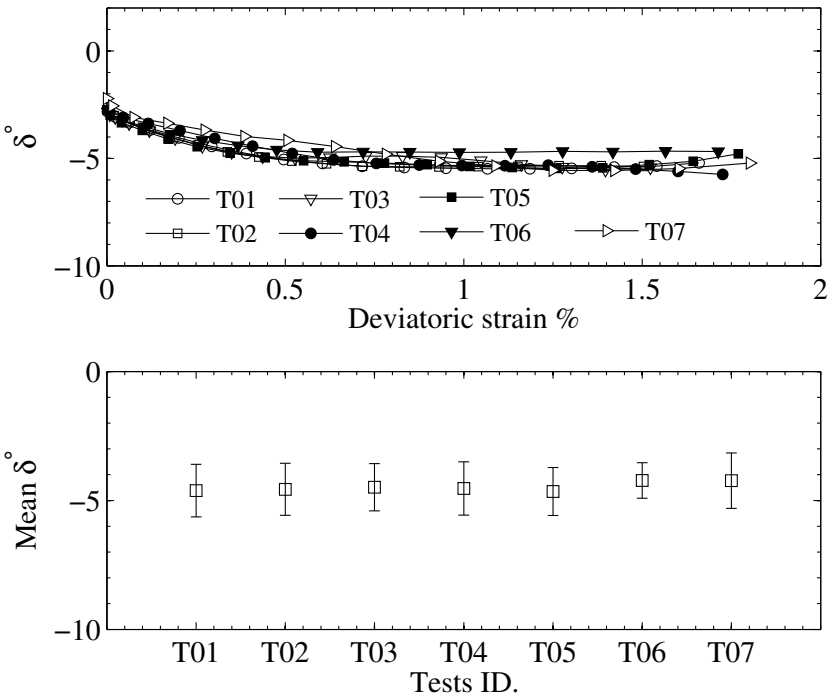

Fig. 39. Evolution of δ during axial compression stage

At the end of the axial compression stage the sample has an anisotropic structure, in terms of $n(v_i)$, while the material axes are closely aligned with those of principal strain/stress. Consider now the loading process involving rotation of principal strain axes, as discussed in Section 3.3.1. During this loading, the material triad also undergoes a progressive rotation and the primary objective here is to establish a correlation between the two.

Fig. 40 shows the evolution of the angle δ with rotation of the principal strain axes, α_ε, for all test considered in the parametric study conducted earlier. The results correspond, once again, to the same fabric descriptor $n(v_i)$. It is observed that in all tests involving $\phi_s = 30^\circ$ and $\phi_s = 40^\circ$ (i.e. tests T02, T03, T05, T06 and T07), the angle δ remains very small for the whole range of $\alpha_\epsilon \in (0^0, 90^0)$. This indicates that there is a coaxiality between the material axes and those of the principal strain over this entire range. The figure at the bottom shows the mean values and the standard deviation of the angle δ for all tests reported in Section 3.3.2. It is noted that, based on results shown in Figs. 32-34, the mobilized friction angle for test T06 is approx. is 29°, which is very close to the friction angle of medium dense Ottawa sand as recorded in drained triaxial compression tests. In this case, there is $\delta = -0.55 \mp 4.58^\circ$, i.e. the deviation of material triad from the principal strain directions during the continuing rotation of principal strain axes is of the same order of magnitude as that for axial compression stage. The same conclusion applies to tests T02, T03 as well as T05. It is observed that the largest values

of δ correspond to cases involving $\phi_s = 20^\circ$, i.e. test T01 ($\delta = 10.93 \mp 6.94^\circ$) and test T04 ($\delta = 10.16 \mp 7.10^\circ$). It is interesting to note, however, that the general predictive abilities of DEM at these low values of ϕ_s are not very convincing. This is evident from Fig.32, whereby the volumetric behavior of specimens in both tests T01 and T04 is typical of that for dense assemblies which are characterized by a significantly larger mobilized friction angle.

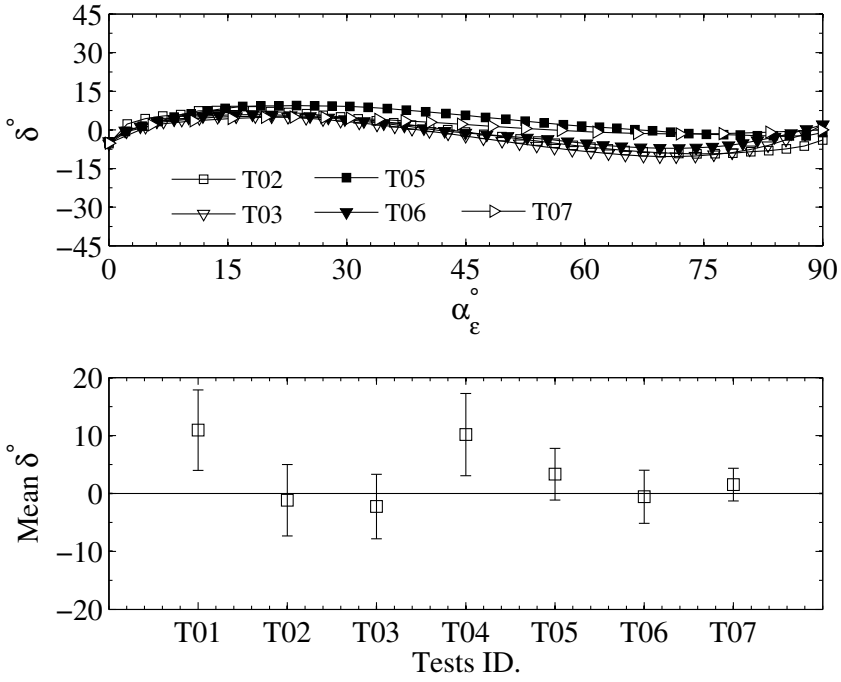

Fig. 40. Evolution of δ during rotation of principal strain axis

Fig. 41 examines the influence of material parameters on the evolution of the angle δ during the rotation of principal strain axes. The top figure, gives the results of

tests T05 and T06. The values of shear stiffness K_S and stiffness ratio K_S/K_N are the same while the inter-particle friction angles ϕ_s are 30° and 40°, respectively. The second figure shows the influence of the stiffness ratio K_S/K_N. Here, the results of tests T03 and T06 for $\phi_s = 40^\circ$ are compared. Note that $K_S/K_N = 0.1$ for T03, while $K_S/K_N = 1$ for the T06 test. The last figure, at the bottom, shows the comparison of the results for tests T05 and T07. In this case, the value of shear stiffness, K_S, in T07 test is 4 times smaller than that in T05 test. It is noted here that, while the evolution of the angle δ is affected by the choice of parameters, the general conclusion pertaining to coaxiality between the material axes and those of the principal strain still remains valid.

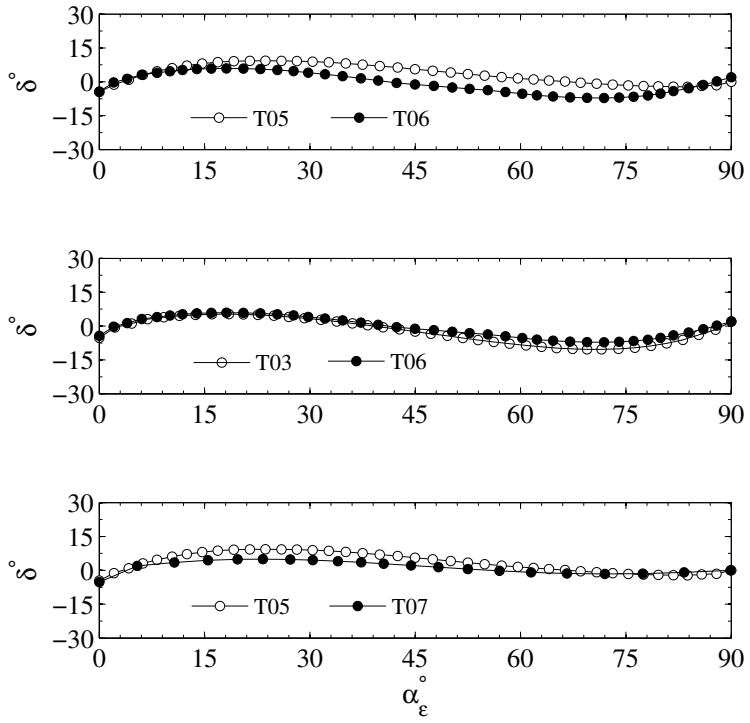

Fig. 41. Influence of material parameters on the evolution of δ during rotation of principal strain axis

Fig. 42 presents the geometric representation of n_{ij}^{Ω} and n_{ij}^{e} tensors during rotation of principal strain axes for test T06. Here, geometric objects (or glyphs) are plotted as superquadric surfaces. Glyphs of tensors n_{ij}^{e} are superimposed on those of tensors n_{ij}^{Ω} in order to provide an immediate visual interpretation of the coaxiality of principal material directions and principal (deviatoric) strain. The semi axes are scaled to maximum of 1 for n_{ij}^{Ω} and $1/2$ for n_{ij}^{e}. It should be noted that since both tensors are

deviatoric, and thus have positive and negative eigenvalues, a four pointed concave shape is used based on the work reported in ref. Schultz and Kindlmann 2010. Different gray-scale is used to show different signs of the eigenvalues.

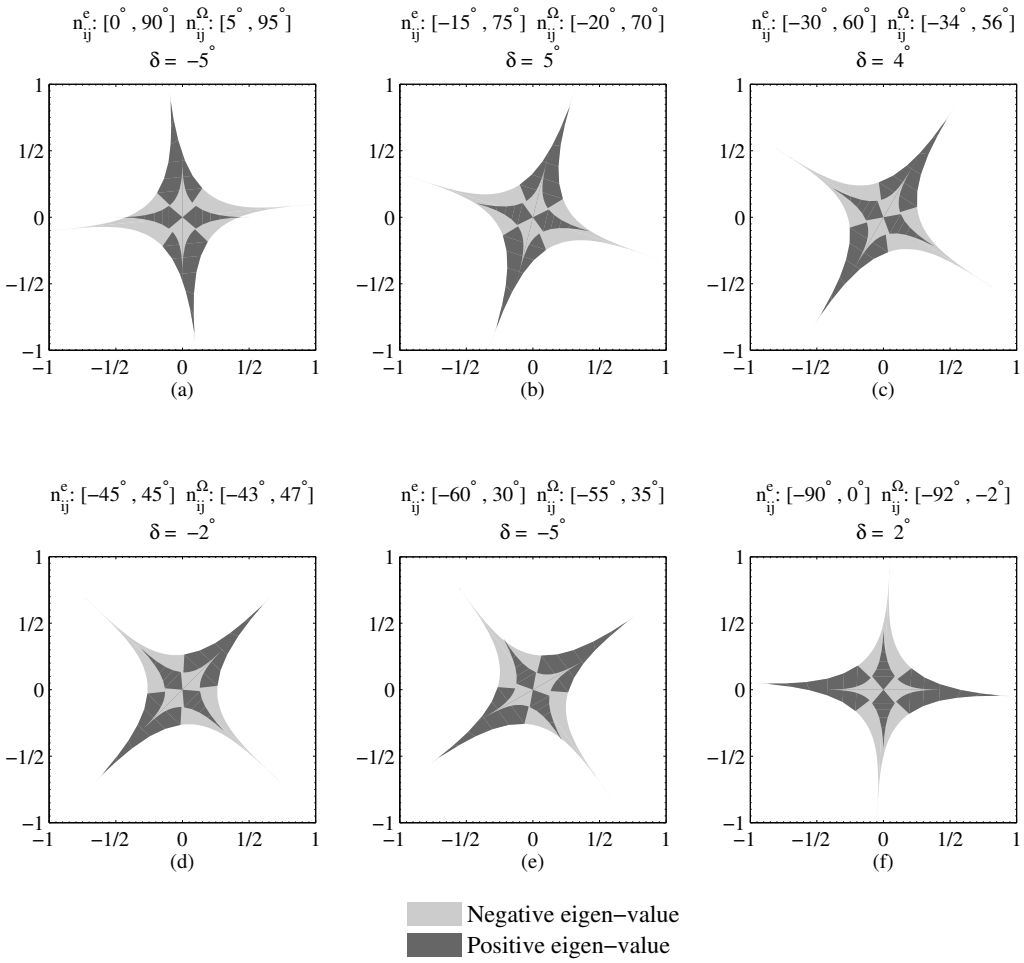

Fig. 42. Evolution of fabric during rotation of principal strain axis: (a) $\alpha_{\varepsilon} = 0^{\circ}$; (b) $\alpha_{\varepsilon} = 15^{\circ}$; (c) $\alpha_{\varepsilon} = 30^{\circ}$;(d) $\alpha_{\varepsilon} = 45^{\circ}$; (e) $\alpha_{\varepsilon} = 60^{\circ}$; (f) $\alpha_{\varepsilon} = 90^{\circ}$

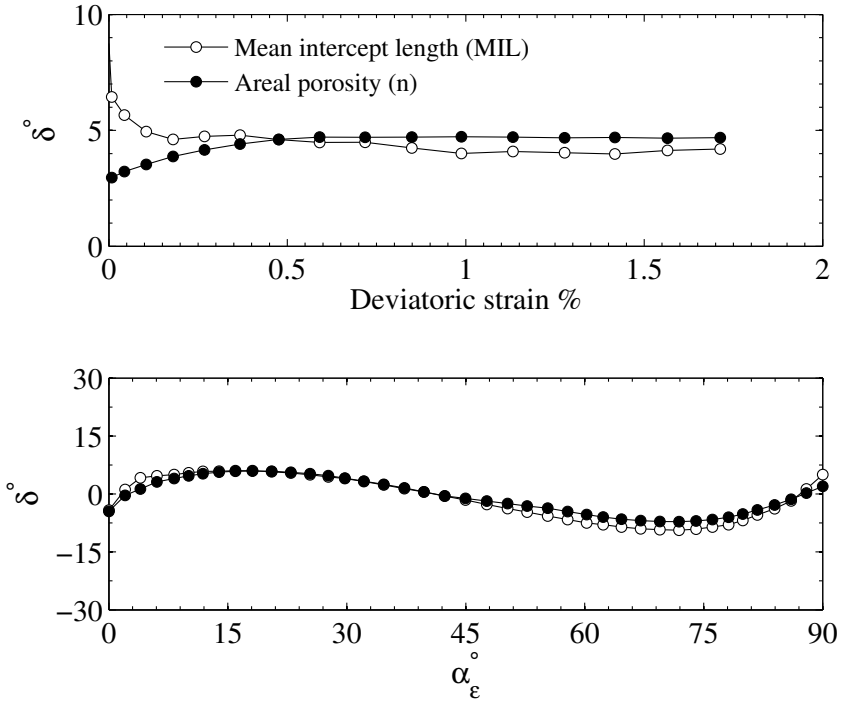

Fig. 43. Comparison of evolution of δ based on *MIL* and n descriptors

Fig. 43 shows the comparison of the results for two different fabric measures as defined in Section 2, i.e. *MIL* and n. The top figure shows the change in δ as a function of continuing deformation during the axial compression stage, while the figure at the bottom gives the evolution of δ in the test involving rotation of the principal strain directions. The results correspond to test T06. It is evident that the overall trends in the evolution of material axes, as predicted by these two measures during the deformation process, are very similar. In particular, during the test involving rotation of principal strain axes, as α_ε approaches 45° the two curves become virtually identical.

Finally, Fig. 44 addresses the issue of evolution of principal directions of fabric, α_Ω, in relation to those of other measures, including stress and strain increments, i.e. α_σ and $\alpha_{\Delta\varepsilon}$. The results correspond to the fabric descriptor n and the test T06. It can be seen here that, at the start of the test, α_σ remains close to α_ε but it deviates significantly in the course of rotation of principal strain axes. After 45° rotation of α_ε, the angle of deviation approaches 30°, which implies that the angle between $\alpha_{\Delta\varepsilon}$ and α_σ is 15°. Thus, it is evident that the notion of coaxiality, as postulated here, applies to the strain and not the stress deviator.

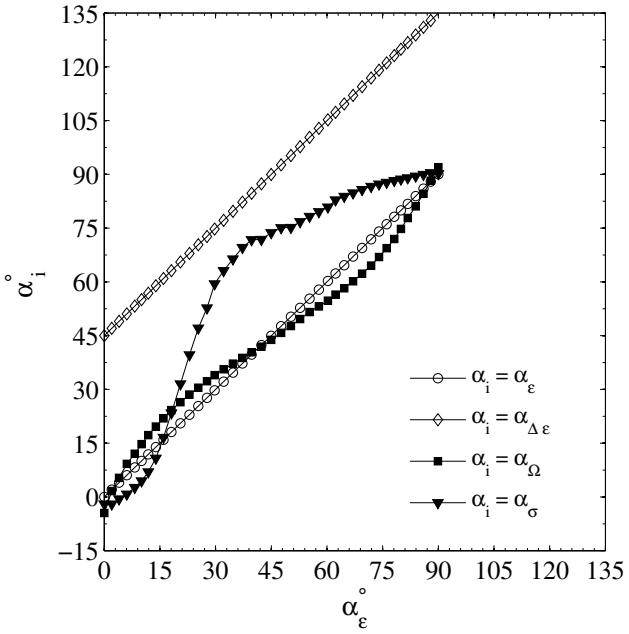

Fig. 44. Evolution of $\alpha_{\Delta\varepsilon}$, α_σ and α_Ω during rotation of principal strain axes

3.5. Numerical examples of mechanical response of granular materials with induced anisotropy

In this section, examples of numerical simulations, demonstrating the influence of induced anisotropy are presented. The material is assumed to have an initially isotropic microstructure, which progressively evolves during the deformation process. The influence of induced anisotropy on the strength characteristics is then described by the variation of the anisotropy parameter η_f, as defined by equation (2.4)

$$\eta_f = \eta_0 \left(1 + \Lambda_{ij} n_i n_j + a_1 \left(\Lambda_{ij} n_i n_j\right)^2 + \ldots\right) \tag{3.14}$$

The tensor Λ_{ij} which governs the bias in spatial distribution of strength parameter η_f, is defined as

$$\Lambda_{ij} = \beta e_{ij} \tag{3.15}$$

where e_{ij} denotes the deviatoric strain tensor which evolves during deformation and β is a constant.

In what follows, the constitutive framework described in Chapter 2 has been applied to simulate the response of Ottawa sand. The experimental data are provided in Chapter 2. The material parameters corresponding to proposed model, have been chosen as

$$\eta_0 = 0.89, A = 0.1\,mm, t = 6mm, \eta_c = 0.65\eta_f, E = 6\,MPa$$

Note that, the hardening parameter A corresponds to $\sigma_n = 10\,kPa$ and the constant η_0 is the mean value of strength parameter η_f, as depicted in Fig. 14 This set of material parameters describes sand in a dense state of compaction. At this stage, the existing experimental evidence is insufficient to identify, in a unique manner, the parameter entering the evolution law. Therefore, the value of parameter β has been selected on a purely intuitive basis.

A series of simulations were carried out first to investigate the influence of parameter β on the mechanical characteristics. The simulations were carried out using a loading history that was similar to the experimental program reported by Arthur et al. (1977) and Wong et al. (1985). In those tests, directional shear cell device was employed to examine the plane strain response of dense sand under controlled changes of principal stress directions. Note that in directional shear cell normal and shear stresses can be independently controlled on four faces of a cubical specimen. Moreover, initial isotropy in the plane of loading can be achieved by pouring sand in the direction normal to this plane. Thus, the effects of inherent and induced anisotropy can be decoupled.

Consider first a sand sample tested under hydrostatic compression of $14\,kPa$. The sample is assumed to be subjected to an increasing axial stress under drained conditions.

The rotation of principal stress directions of a prescribed magnitude $\Delta\psi$ with respect to the orientation of the previous principal stress system is then applied.

The analysis has been conducted for three different values of parameter $\beta = 0.1, 5, 10$. The tests were simulated for $\Delta\psi = 0^\circ$ and 90°.

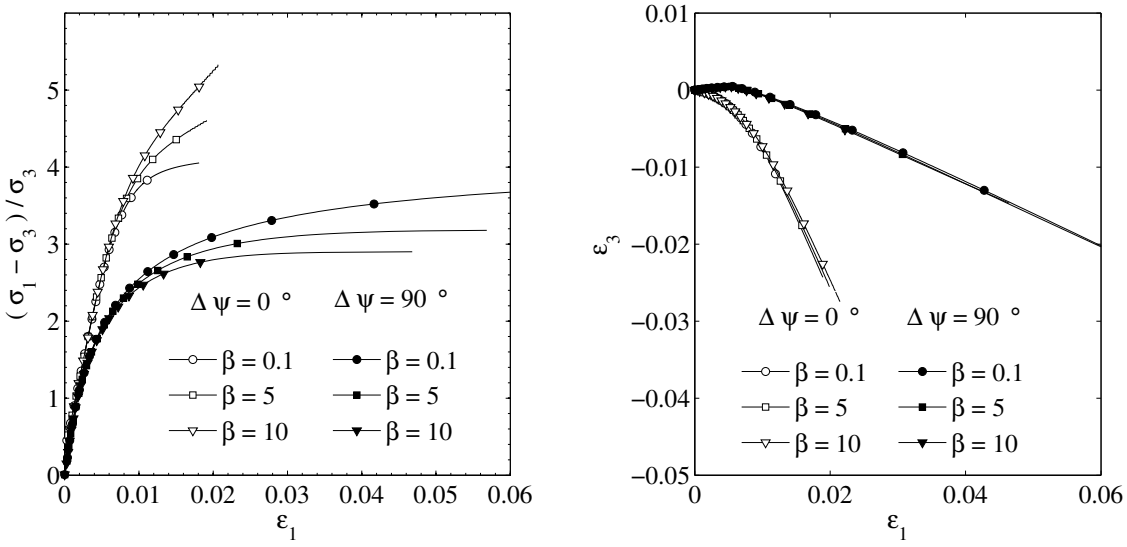

Fig. 45. Effects of previous loading on induced anisotropy with different values of constant β $\Delta\psi = 0^\circ$ and $\Delta\psi = 90^\circ$; (a) Strength characteristics; (b) Deformation characteristics

Figs. 45a and 45b show the predicted strength characteristics and corresponding deformation characteristics. It is seen from Fig. 45 that stiffness moduli prior to failure remain affected by the orientation of the sample. In general, the sample tested at $\Delta\psi = 0^\circ$ displays a stiffer response as compared to that tested at $\Delta\psi = 90^\circ$. Once again, the results

are in qualitative agreement with those published in the literature. It is also seen that by increasing the value of the parameter β more difference in strength is obtained.

Figs. 46a and 46b show the mechanical characteristics obtained for samples tested at different values of rotation of principal stress axes corresponding to $\Delta\psi = 0^{\circ}$, 45° and 90°, with parameter β fixed at $\beta = 0.1$, respectively. The most notable feature of the simulations is the increase in the value of major principal strain on reloading (e.g. after a principal stress rotation $\Delta\psi$ is applied), which is consistent with experimental data.

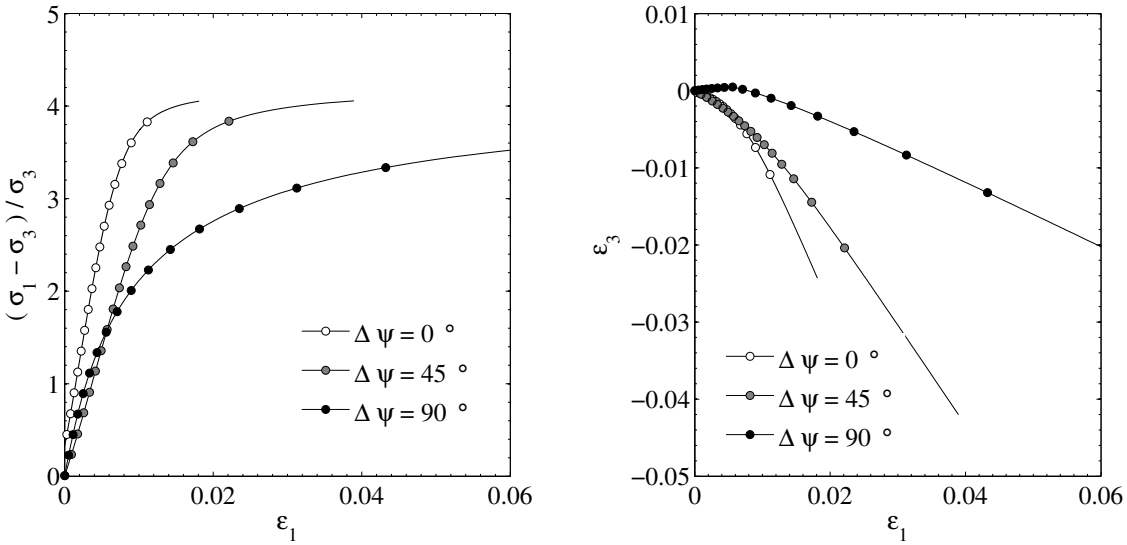

Fig. 46. Effects of previous loading on induced anisotropy: $\Delta\psi = 0^{\circ}$, $\Delta\psi = 45^{\circ}$ and $\Delta\psi = 90^{\circ}$ with constant $\beta = 0.1$; (a) Strength characteristics; (b) Deformation characteristics

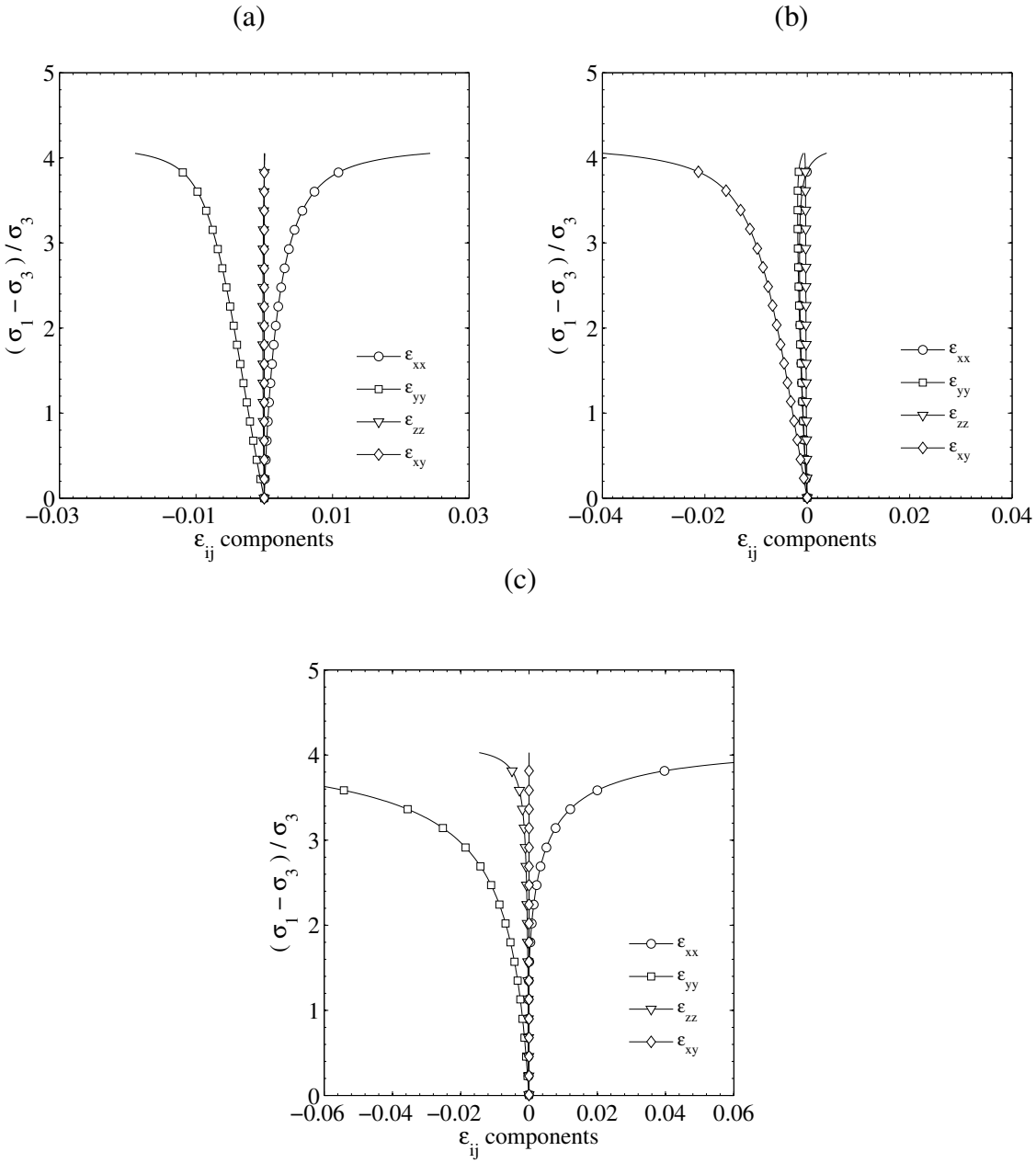

Fig. 47. Variations of ε_{ij} components; (a) $\Delta\psi = 0^{\circ}$; (b) $\Delta\psi = 45^{\circ}$; (c) $\Delta\psi = 90^{\circ}$ with constant $\beta = 0.1$

Fig 47a, 47b and 47c illustrate the evolution of all strain components. Unfortunately, variations in other strain components were not reported in the original reference, so that no qualitative comparison is feasible.

3.6. Final remarks

Granular materials are often anisotropic in nature. The anisotropy may stem from the shape of the grains within the specimen, in which case it's referred to as inherent. Even though a granular material may be isotropic in terms of grain architecture, there is usually a bias in the distribution of void space due to initial compaction, which leads to anisotropy that may evolve during the deformation process. For characterization of deformation-induced anisotropy, some measures of material fabric are required. Stereology-based fabric measures, whose principal directions are coincident with the principal axes of microstructure, are considered to be the most appropriate. In case of induced anisotropy, the formulation of the problem requires a relation that defines the evolution of the principal axes of microstructure during the deformation process. It is postulated here that such an evolution law may be formulated by imposing coaxiality between the microstructure and the strain tensors.

In this work, a numerical study has been conducted using Discrete Element Method (DEM) to investigate the evolution of internal structure of a two-dimensional particulate assembly. The assembly examined here exhibits similar qualitative trends in

the mechanical response to those of a real granular material. A parametric study was conducted with the aim of determining the influence of material parameters on material characteristics. The validity of postulated evolution law was then examined for all cases considered in the parametric study.

The results clearly indicate that for a dense two-dimensional assembly of rigid spherical particles the evolution law may incorporate an assumption of coaxiality of principal directions of microstructure and the strain tensor. It is noted that the two-dimensional DEM model is representative of a three dimensional medium composed of cylinders of constant thickness or spheres whose centroids all lie in the same plane. Although the conclusions emerging from this work are belied to be fairly general, the validity of the postulated form of the evolution law needs to be further examined in the context of a 3D granular assembly.

APPENDICES

APPENDIX A

Sample generation

In order to construct a sample which can serve as a REV, both the geometric entities (i.e. particle shape and particle size distribution) and mechanical properties (e.g. contact stiffnesses and interparticle friction coefficient) must be specified. In this study, the gradation curve corresponding to Ottawa standard sand (C109), which is quartz sand with sub-rounded to rounded particles, is reproduced. The sample is idealized as an assembly of circular particles enclosed by rigid platens as shown in Fig. A. 1. The sample is generated by random creation of non-contacting particles whose particle size follows the Particle Size Distribution (PSD) curve of Ottawa sand. Particles with an initially reduced radius are randomly generated inside the boundary segments prior to their subsequent radius expansion. An important aspect of the sample formation is the generation of the random configuration of particles, which satisfies the basic statistical characteristics of the real material. In general, for a given type of particles whose shape has been prescribed, two major factors need to be considered, i.e. the size distribution and the spatial distribution of particles. The random configuration must be macroscopically

homogeneous and isotropic. The particle size distribution is one of the primary factors affecting how a soil behaves under mechanical load. It should be noted that the particle size distribution determined from sieve analysis describes a size distribution based on particle mass. However, the particle size distribution for an assembly of particles in DEM is based on the number of particles within each grading segment, assuming all particles have equal density.

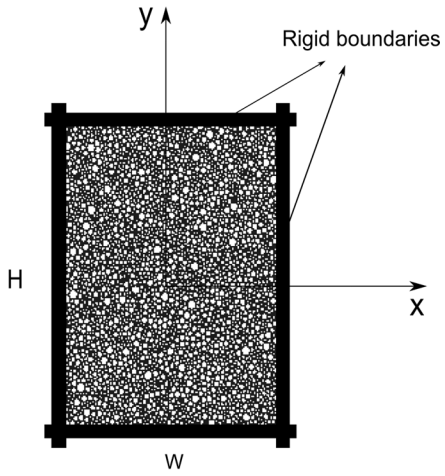

Figure A. 1. Sample configuration

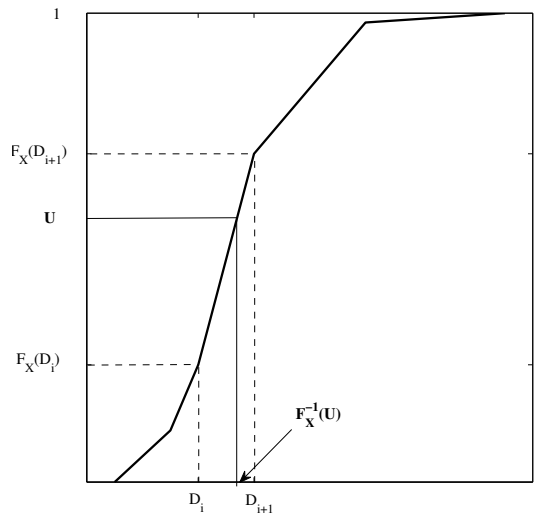

Figure A. 2. Schematic diagram of particle size distribution

In order to produce a random particle configuration, Smirnov transform (also known as inverse transform sampling) is carried out by taking particles from a source whose size distribution follows a given Particle Size Distribution (PSD) curve, Fig. A. 2, and placing them one by one in such a way that there is no overlapping and the spatial distribution is as macroscopically homogeneous as possible. The key steps of the random generation scheme adopted in this work are listed below.

- Divide the given PSD curve into segments. In Fig. A. 2, D_{i+1} and D_i represent the maximum and the minimum diameter of a given grading segment, respectively.

- In order to generate a random number defining the size of the particle, the inverse transform sampling is employed. Inverse transform sampling is a way of

generating samples for a random variable X from distribution function $F_X(x)$. $F_X(x)$ may be expressed in terms of the probability density function $f_X(x)$, i.e.

$$F_X(x) = \int_{-\infty}^{x} f_X(x)dx \qquad \text{A. 1}$$

for continuous random variables, and

$$F_X(x_j) = \sum_{i=0}^{j} P_i \qquad \text{A. 2}$$

for discrete random variables where $P(X = x_j) = P_j$, $j = 0,1,\ldots,m$. If U is uniformly distributed over the interval $(0,1)$, it can be proven that

$$X = F_X^{-1}(U) \qquad \text{A. 3}$$

Thus, in order to get a sample, say x, of a random variable X, one can obtain a sample, say u, of a random variable U, compute $F_X^{-1}(u)$, and set it equal to x.

- A uniform probability distribution is assumed for the particles centers. A random number generator is used to generate the pairs of coordinates (x_i, y_i) of the particle centers: $x_i = X_{min} + \eta_1 (X_{max} - X_{min})$ and $y_i = Y_{min} + \eta_2 (Y_{max} - Y_{min})$, where

$X_{min}, X_{max}, Y_{min}, Y_{max}$ are the minimum and the maximum X, Y coordinates of the rectangular area under consideration. Here, η_1 and η_2 are two independent random numbers uniformly distributed between 0 and 1.

- For each generated coordinate pair, possible overlaps of the new particle with the previously placed particles and with the specimen boundaries are then checked. The coordinate pair is rejected if an overlap occurs.

The histogram of generated samples and the corresponding cumulative distribution function (CDF) are shown in Figs. A. 3 and A. 4, respectively. The CDF closely follows the prescribed PSD curve, as shown in Fig. A. 4.

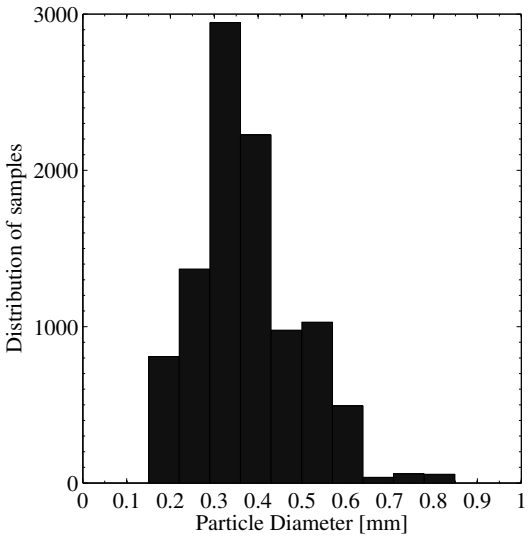

Figure A. 3. Histogram of samples

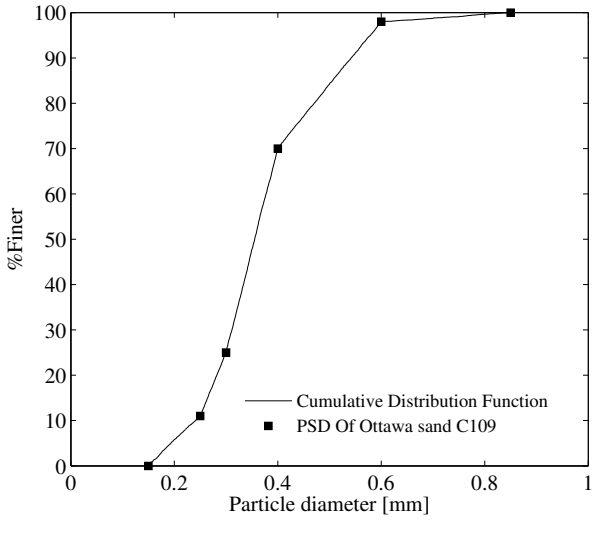

Figure A. 4. Comparison of CDF of generated particles with the given PSD curve

The particle assembly generated by the procedure above, has a high porosity while the particles themselves are not in contact. A compact particle system is then generated according to the radius expansion procedure (O'Sullivan 2011) and a DEM solution cycle to reach a steady state assembly. The coefficient of friction is set to 0 during the radius expansion. The evolution of the stress state and the coordination number during the radius expansion are shown in Figs. A. 5 and A. 6. At the end of the radius expansion process, the coordination number is 3.83 which is very close to the upper bound limit of 4 reached by an isostatic (rigid) structure. According to Roux (2000), the coordination number of a system of frictionless spheres at equilibrium is equal to $2d$ for dimension d .

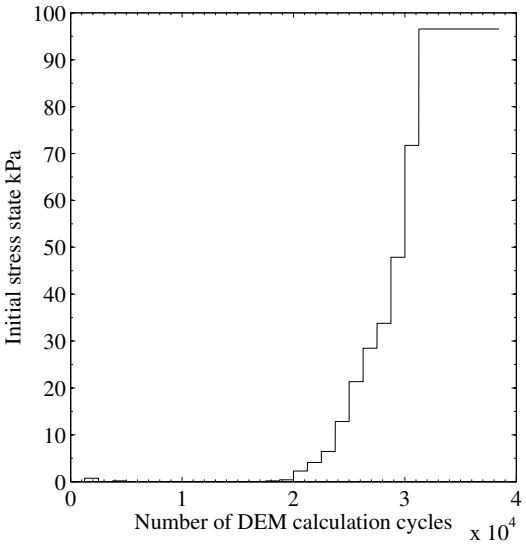

Figure A. 5. Evolution of initial stress state during radius expansion

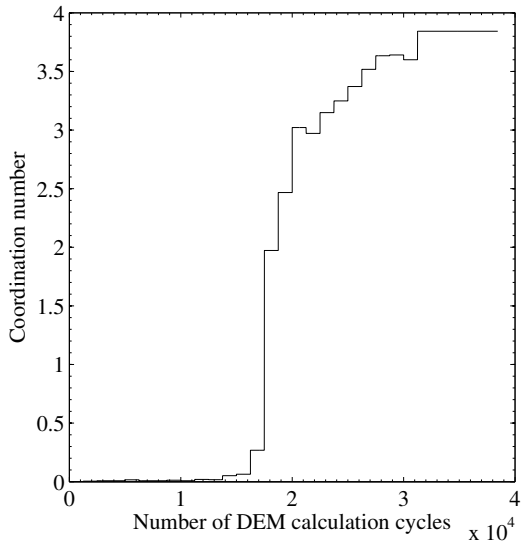

Figure A. 6. Evolution of coordination number during radius expansion

An isotropic compression test is then conducted in order to bring the particle assembly to the initial stress state of $100kPa$, using a numerical servo-control mechanism.

APPENDIX B

General methodology for DEM analysis

In the DEM a continuum is replaced by an assembly of rigid/deformable particles that interact with each other through contact points or contact interfaces. The global deformation under an increment of load causes the particles in the assembly to move relative to each other. Considering each particle to have six degrees of freedom, i.e. three translational and rotational respectively, the relative displacement $\Delta\delta_i$ at the contact of any two particles p and q is given by (Chang and Misra 1990)

$$\Delta\delta_i = \Delta u_i^p - \Delta u_i^q + e_{ijk}(\Delta\omega_j^p r_k^p - \Delta\omega_j^q r_k^q) \qquad \text{B. 1}$$

while the relative rotation $\Delta\theta_i$ at the contact is given by

$$\Delta\theta_i = \Delta\omega_i^p - \Delta\omega_i^q \qquad \text{B. 2}$$

where Δu_i, $\Delta\omega_i$, Δr_k and Δe_{ijk} denote particle displacement, particle rotation, the vector joining the particle centroid to the contact point and permutation symbol respectively. The increment of relative displacement $\Delta\delta_i$, is related to the increment of contact forces Δf_i through the constitutive relation K_{ij} as

$$\Delta f_i = \mathrm{K}_{ij}\Delta\delta_j \qquad \text{B. 3}$$

Assuming that there is no coupling between the shear and normal displacement components, one can write

$$\mathrm{K}_{ij} = \mathrm{K}_{\mathrm{N}} n_i n_j + \mathrm{K}_{\mathrm{S}}(s_i s_j + t_i t_j) \qquad \text{B. 4}$$

where K_{N} and K_{S} are normal and tangential contact stiffnesses and the vector n_i denotes unit contact normal while the base vectors s_i and t_i are chosen arbitrarily to form a right handed orthogonal system. For particular media, the rotational stiffness may be neglected, since the area of contact is negligibly small. Forces due to the particle momentum are also neglected since the granular system is assumed to undergo a significant deformation under quasi-static conditions.

Distinct element programs use explicit time-marching scheme to solve the equations of motion directly. For each particle, the following equations are integrated twice by central finite difference:

$$\begin{aligned} m\ddot{u}_i + \alpha m\dot{u}_i &= \sum F_i \\ I_{(i)}\ddot{\theta}_i + \alpha I_{(i)}\dot{\theta}_i &= \sum M_i \end{aligned} \qquad \text{B. 5}$$

where $\ddot{u}_i$ and $\dot{u}_i$ are components of linear acceleration and velocity, $\ddot{\theta}_i$ and $\dot{\theta}_i$ are components of angular acceleration and velocity, $\sum F_i$ and $\sum M_i$ are sum of forces and sum of moments acting on particle, m and α denote mass of particle and damping coefficient and $I_{(i)}$ denote moments of inertia with respect to chosen coordinate axis.

The calculations performed in the DEM involve the application of Newton's second law to the particles and the force-displacement law at the contacts. Newton's second law is used to determine the motion of each particle arising from the contact and forces acting upon it, while the force displacement law is used to update the contact forces arising from the relative motion at each contact.

To capture the response for contact interaction at the contact points, a variety of contact laws have been proposed. In the current study the soft particle model proposed by Cunall and Strack (1979), has been used.

i. Normal contact forces law

Two circular particles with radii r_p and r_q , respectively interact only if they are in contact so their overlap

$$\Delta = (r^p + r^q) - (x_i^p - x_i^q)n_i \qquad \text{B. 6}$$

is positive $\Delta > 0$, with the unit vector $n_i = (x_i^p - x_i^q)/|\, x_i^p - x_i^q \,|$, pointing from p to q. The contact force between particle p and q can be decomposed into normal and tangential parts, i.e. $f_i^c = f_N n_i + f_T t_i$ where $n_i t_i = 0$.

The normal contact force model involves a linear repulsive and a linear dissipative force,

$$f_{\mathrm{N}} = \mathrm{K_N}\Delta + \gamma v_{\mathrm{N}} \qquad \text{B. 7}$$

with a spring stiffness $\mathrm{K_N}$, a viscous damping γ and the relative velocity in normal direction $v_{\mathrm{N}} = -\left(v_i^p - v_i^q\right)n_i$. This so-called linear spring dashpot model views the particle contact as a damped harmonic oscillator.

ii. Tangential contact forces law

The tangential forces are computed from the accumulated sliding of the contact points. In sliding frictional model, the tangential force is coupled to the normal force via Coulombs law: $f_{\mathrm{T}} \le \mu_s f_{\mathrm{N}}$. The tangential contact force can be defined as

$$f'_{\mathrm{T}} = \mathrm{K_T}\,\zeta \qquad \text{B. 8}$$

with the tangential stiffness $\mathrm{K_T}$ and tangential contact displacement ζ, which is updated as

$$\zeta = \zeta + v_{\mathrm{T}}\Delta t \qquad \text{B. 9}$$

As long as $f_{\mathrm{T}} \le f_C$, with $f_C = \mu_s f_{\mathrm{N}}$, one has static friction and on the other hand if the limit $f_{\mathrm{T}} > f_C$ is reached sliding friction is active. The tangential contact law reads,

$$f_{\mathrm{T}} = -min(f_C, f'_{\mathrm{T}}) \qquad \text{B. 10}$$

APPENDIX C

Definition of stress/strain operators

The definition of stress and strain tensors are based on the volume averaging technique outlined in the article by Li et al. (2013).

i. Stress tensor

In order to define the average stress tensor for the assembly of particles, the volume averaging method was used. With the assumptions of internal stress uniformity and macroscopic homogeneity, the traction vector t_i acting on the surface with unit normal n_i, is related to the Cauchy stress tensor σ_{ij} through: $t_i = \sigma_{ij} n_j$. In the absence of body forces, the equations for equilibrium are $\sigma_{ij,j} = 0$. The average stress in volume V is defined as:

$$\sigma_{ij} = \frac{1}{V} \int_V \sigma_{ij} dV \qquad \text{C. 1}$$

since $\sigma_{ij} = \sigma_{kj} \delta_{ik} = \sigma_{kj} x_{i,k}$, equation (C. 1) may be written as

$$\sigma_{ij} = \frac{1}{V} \int_V [(\sigma_{kj} x_i)_{,k} - x_i \sigma_{kj,k}] dV \qquad \text{C. 2}$$

by substituting $t_i = \sigma_{ij} n_j$, into the above equation and using Gauss's divergence theorem, equation (C. 1) can be transformed into

$$\sigma_{ij} = \frac{1}{V} \int_S x_i t_i dS \qquad \text{C. 3}$$

The surface integral in equation (C. 3) can then replaced by a sum over the μ discrete forces T^m acting at the boundary, to give,

$$\sigma_{ij} = \frac{1}{V} \sum_{m=1}^{\mu} x_i^m T_j^m \qquad \text{C. 4}$$

The average stress can be also evaluated based on contact forces between particles, within volume V as,

$$\sigma_{ij} = \frac{1}{V} \sum_{c=1}^{N_c} l_i^c T f_j^c \qquad \text{C. 5}$$

where l_i^c (the branch vector for contact c) connects particles a and b with centroid coordinates x_i^{pa} and x_i^{pb}, i.e.

$$l_i^c = \left| x_i^c - x_i^{pa} \right| n_i^{c,pa} - \left| x_i^c - x_i^{pb} \right| n_i^{c,pb} \qquad \text{C. 6}$$

Note that $n_i^{c,pa}$ and $n_i^{c,pb}$ are the unit vectors directed from centroids of particles a and b to the contact point c, respectively.

ii. Strain tensor

Let x_i and X_J be the current and reference positions of a material point. Moreover, let the deformation gradient $\partial x_i / \partial X_J$ be denoted by F_{iJ}. With the assumption of uniformity of the strain field at the macroscale, the average deformation gradient over a volume V enclosed by the surface S is defined as

$$F_{iJ} = \frac{1}{V}\int_V x_{i,J}\, dV \qquad \text{C. 7}$$

by use of Gauss's divergence theorem, equation (C. 7) can be transformed into:

$$F_{iJ} = \frac{1}{V}\int_S x_i\, N_J\, dS \qquad \text{C. 8}$$

where N_J are the components of the outward normal vector to the surface S. In two-dimensional case, equation (C. 8) can be written as,

$$F_{iJ} = \frac{1}{V}\int_S x_i\, e_{JK}\, \frac{dX_k}{dL}\, dL \qquad \text{C. 9}$$

in which e_{JK} is the $2D$ permutation tensor. By integrating by parts, equation (C. 9) can be transformed into,

$$F_{iJ} = e_{JK}\,\frac{1}{V}\int_S [d(x_i X_K) - X_K\,dx_i] \qquad \text{C. 10}$$

The compatibility condition along the boundary implies

$$d(x_i X_K) = 0 \qquad \text{C. 11}$$

Hence,

$$F_{iJ} = \frac{1}{V} e_{JK} \int_S X_K\,dx_i \qquad \text{C. 12}$$

The surface integral again can be replaced by a sum over the β boundary segments as

$$F_{iJ} = \frac{1}{V} e_{JK} \sum_{n=1}^{\beta} X_K^{\beta} \Delta x_i^{\beta} \qquad \text{C. 13}$$

in which X_K^{β} denotes the coordinates of the center of the boundary segment β in the initial configuration and Δx_i^{β} is the relative position of the two vertices of the boundary segment β after deformation.

The average deformation gradient that defines the measure of average strain can be expressed as,

$$\varepsilon_{IJ} = \frac{1}{2}\left(F_{IJ} + F_{JI}\right) - \delta_{IJ} \qquad \text{C. 14}$$

Noting that, the displacement vector is defined as $u_i = x_i - X_J \delta_{Ji}$ and substituting equation (C. 13) into equation (C. 14), the average strain tensor can be defined as

$$\varepsilon_{IJ} = \frac{1}{V} e_{IL} \delta_{KJ} \sum_{n=1}^{\beta} X_L^{\beta} \Delta u_k^{\beta} \qquad \text{C. 15}$$

APPENDIX D

Specification of the kinematics of boundary segments

The following procedure has been employed to determine translational and rotational velocities of boundary segments (Li et al. 2013). According to equation (C. 15) in Appendix C, in a strain field ε_{IJ}, a vector δX_I in the initial configuration is transformed into

$$\delta x_i = F_{iJ}\delta X_J = \delta_{iK}(\delta_{JK} - \varepsilon_{JK})\delta X_J \qquad \text{D. 1}$$

in the deformed configuration. Fixing the position of specimen origin O, the position of a material point X_I in the deformed configuration can be determined as

$$x_i = F_{iJ}\delta X_J = \delta_{iK}(\delta_{JK} - \varepsilon_{JK})X_J \qquad \text{D. 2}$$

In the analysis, it is necessary to specify the geometry of rigid boundary segments by defining their centers and normal vectors. These quantities are denoted as X_O^β, N_O^β (in the initial configuration), and x_O^β, n_O^β (in the deformed configuration), respectively, and are specified as

$$N_O^\beta = \frac{T_1^\beta \times T_2^\beta}{\left|T_1^\beta \times T_2^\beta\right|} \; ; n_O^\beta = \frac{t_1^\beta \times t_2^\beta}{\left|t_1^\beta \times t_2^\beta\right|} \qquad \text{D. 3}$$

Note that two in-plane vectors T_1^{β} and T_2^{β} (in the initial configuration), and t_1^{β} and t_2^{β} (in the deformed configuration) should be used to determine N_O^{β} and n_O^{β} .

Finally, to apply a strain increment $\Delta\varepsilon_{IJ}$ during a time step Δt, the translational and rotational velocities of boundary segments are specified as

$$v_i^{\beta} = \frac{x_i^{\beta}}{\Delta t} = -\frac{\delta_{iK}\,\Delta\varepsilon_{JK} X_{OJ}^{\beta}}{\Delta t} \qquad \text{D. 4}$$

and

$$w_i^{\beta} = \frac{n^{\beta} \times n^{\beta t}}{\Delta t} \qquad \text{D. 5}$$

CHAPTER 4. CONCLUSIONS AND RECOMMANDATIONS

4.1. Summary and conclusions

The study presented here includes both the experimental and numerical aspects and it provides a comprehensive insight into the anisotropic response of granular materials.

The experimental investigations were conducted on Ottawa standard sand C109 that comprises nearly rounded particles. To induce a distinct microstructure, a sand rain method followed by a densification process was used for sample preparation which enabled uniform anisotropic specimens to be produced at the selected void ratio. The material tests involved direct shear and triaxial experiments and were aimed at examining the effects of inherent anisotropy on both the deformation and strength characteristics.

A numerical study has been conducted using Discrete Element Method (DEM) to investigate the evolution of internal structure of a two-dimensional particulate assembly. An evolution law was then formulated by postulating coaxiality between the microstructure and the total strain tensors.

A general constitutive framework was outlined which is capable to model the effects of inherent anisotropy in particulate media. The incorporation of the proposed

evolution law into this framework results in a constitutive law that can also describe, at least in a qualitative manner, manifestation of induced anisotropy in granular materials.

4.2. Recommendations for future work

The methodology presented here, can be incorporated into finite element framework for solving complex boundary value problems that involve granular materials with inherent/induced anisotropy. It is well known that, in practical geotechnical problems such as, tunnel excavation, slopes, foundations, etc., continuous rotation of principal stress directions occurs and has a considerable influence on deformation and strength behavior of soil mass.

Different elasto-plastic constitutive theories, rather than deviatoric hardening which is used in this study, can also be incorporated into the framework in order to model the mechanical characteristics of other geomaterials such as clays and rocks. Clays may become anisotropic as a result of consolidation process, while the anisotropy in rocks may be inherent (sedimentary rocks) or induced by the deformation process (onset and propagation of fractures). A conceptually similar methodology to the one outlined here, may be followed to describe the deformation characteristics of these geomaterials.

REFERENCES

Arthur JRF, Bekenstein S, Germaine JT, Ladd CG. Stress path tests with controlled rotation of principal stress directions. RN. Yong, FC. Townsend (Eds.), *Laboratory shear strength of soil*, ASTM STP 740, ASTM, Philadelphia, PA. 1981; 516–540

Arthur JRF, Chua KS, Dunstan T. Induced anisotropy in sands. *Geotechnique*. 1977; **27**: 13–33

Azami A, Pietruszczak S, Guo P. Bearing capacity of shallow foundations in transversely isotropic granular media. *International Journal for Numerical and Analytical Methods in Geomechanics*. 2010; **34**: 777–793

Bardet JP, Proubet J. A numerical investigation of the structure of persistent shear-bands in granular media. *Geotechnique*.1991; **41** (4), 599–613

Bardet JP. Experimental Soil Mechanics. *Prentice Hall.* 1997

Bazant ZP, Caner FC, Carol I, Adley MD, Akers SA. Micro-plane model M4 for concrete. I: Formulation with work-conjugate deviatoric stress." *J. Eng. Mech.* 2000; **126**(9); 944–953.

Bazant ZP, Prat PC. Creep of anisotropic clay: New micro-plane model. *J. Eng. Mech.*

1987; **113**(7): 1050–1064.

Boehler P, Sawczuk J. Equilibre limite des sols anisotropes. *Journ. de Mecanique*. 1970.

Boehler JP, Sawczuk A. On yielding of oriented solids. *Acta Mechanica*. 1977; **27**(1−4): 185−206

Butterfield R, Harkness RM, Andrawes KZ. A stereo-photogrammetric method for measuring displacement fields. *Geotechnique*. 1970; **20** (3), 308–314

Calvetti F, Combe G, Lanier J. Experimental micro-mechanical analysis of a 2D granular material: Relation between structure evolution and loading path, *Mechanics of Cohesive-Frictional Materials*. 1997; **2**: 121–163

Calvetti F, Limitations and Perspectives of the Micromechanical Modelling of Granular Materials. *Mathematical and computer modeling*. 2003; **37**: 485–495

Carol I, Jirasek M, Bazant Z. A thermodynamically consistent approach to micro-plane theory. Part I. Free energy and consistent micro-plane stresses. *Int. J. Solids Struct*. 2001; **38**: 2921–2931.

Chang C, Misra A. Packing structure and mechanical properties of granulates. *J Eng. Mec*. 1990; 116: 1077–1093

Chen L, Liu YM, Shao JF. Coupling between inherent and induced anisotropies in sedimentary rocks. *Rock Mechanics: Achievements and Ambitions* edited by Cai M. 2012;81–86

Cundall PA, Strack ODL. A discrete numerical model for granular assemblies, *Geotechnique*. 1979; **29** (l): 47– 65

Dantu P. Etude statistique des forces intergranulaires dans un milieu pulverulent, *Geotechnique.* 1968; **18**, 59–55,

Desrues J, Chambon R, Mokni M, Mazerolle F. Void ratio evolution inside shear bands in triaxial sand specimens studied by computed tomography, *Geotechnique*. 1996; **46** (3):1–18

Doanh T, Dubujet PH, Protie`re X. On the undrained strain-induced anisotropy of loose sand**.** *Acta Geotechnica.* 2013; **8**: 293–309

Doanh T, Dubujet Ph, Touron T. Exploring the undrained induced anisotropy of Hostun RF loose sand. *Acta Geotech*. 2010; **5**(4): 239–256

Doanh T, Finge Z, Boucq S. Effects of previous deviatoric strain histories on the undrained behavior of Hostun RF loose sand. *Geotechnical and Geological Engineering*. 2012; **30**(4): 697–712

Doanh T, Ibraim E, Matiotti R. Undrained instability of very loose Hostun sand in triaxial compression and extension. Part 1: experimental observations. *Mech Cohes Mater*. 1997; **2**(1):47–70

Drescher A, Jong GD. Photoelastic verification of mechanical model for the flow of granular materials. *Journ. Mech. Phys. Solids.* 1972; **20**: 337–351.

Duveau G, Shao JF, Henry JP. Assessment of some failure criteria for strongly

anisotropic materials. *Mechanics of Cohesive Frictional Materials*. 1998; **3**(1): 1–26

Harrigan T, Mann R. Characterization of micro structural anisotropy in orthotropic materials using a second rank tensor. *Journ. Mater. Sci.* 1984; **19**: 761–767.

Haruyama M. Anisotropic deformation strength characteristics of an assembly of spherical particles under three dimensional stresses. *Soils and Foundations*. 1981; **21**(4): 41–55

Hicher PY, Lade PV. Rotation of principal directions in Ko-consolidated clay. J Geotech Eng ASCE. 1987; **113**(7): 774–788

Hight DW, Gens A, Symes MJPR. The development of a new hollow cylinder apparatus for investigating the effects of principal stress rotation in soils. *Geotechnique*. 1983; **33**(4): 355–383

Hill R. The mathematical theory of plasticity. *Oxford University Press.* 1950.

Hoek E, Brown ET. Empirical strength criterion for rock masses. *Journal of Geotechnical Engineering Division*, ASCE. 1980; **106**:1013–1035.

Hoek E. Strength of jointed rock masses. *Geotechnique*. 1983; **33**:187–205

Hong WP, Lade PV. Elasto-plastic behavior of K_o-consolidated clay in torsion shear test. Soil Found. 1989: 29(2): 57–70

Ibrahim E, Lanier J, Muir Wood D, Viggiani G. Strain path controlled shear tests on an analogue granular material. *Geotechnique.* 2010; **60**(7): 545–559.

Inglis D, Pietruszczak S. Characterization of anisotropy in porous media by means of

linear intercept measurements. *Intern. Journ. Solids and Structures.* 2003; **40**: 1243–1264.

Ishihara K, Okada S. Effects of large pre-shearing on cyclic behavior of sand. *Soils Found*. 1982; **22**(3): 109–125

Ishihara K, Okada S. Effects of stress history on cyclic behavior of sand. *Soils Found*. 1978; **18**(4): 31–45

Ishihara K, Okada S. Yielding of overconsolidated sand and liquefaction model under cyclic stresses. Soils Found. 1978; 18(1): 57–72

Iwan, W. D. _1967_. "On a class of models for the yielding behavior of continuous and composite systems." J. Appl. Mech., 34, 612–617

Jamiolkowski M, Ladd CC, Germaine JT, Lanellotta R. New Developments in Field and Laboratory Testing of Soils. *11th Intl. Conf. Soil Mechs. and Foundn. Engrg.,* San Francisco. 1985; 1:57–155

Kanatani K. Distribution of directional data and fabric tensor. *Int. J. Engng Sci*. 1985 ; **22**: 149–161

Kanatani K. Measurement of crack distribution in a rock mass from observations of its surface. *Soils and Found*. 1985: **25**:20–35

Kanatani K. Procedures for stereological estimation of structural anisotropy. *Int. J. Engng Sci.* 1985; **23**: 587–598

Kuo CY, Frost JD, Chameau JL. Image analysis determination of stereology based fabric tensors. *Géotechnique.* 1989; **48**(4): 515–525.

Lade PV, Nam J, Hong WP. Shear banding and cross-anisotropic behavior observed in laboratory sand tests with stress rotation. *Canadian Geotechnical Journal*. 2008; **45**(1): 74–84

Lade PV. Torsion shear apparatus for soil testing. RN. Yong, FC. Townsend (Eds.), *Laboratory shear strength of soil*, ASTM STP 740, ASTM, Philadelphia, PA. 1981; 145–163

Lade VP, Rodriguez NM, and Dyck EJV. Effects of Principal Stress Directions on 3D Failure Conditions in Cross-Anisotropic Sand. *Journal of Geotechnical and Geoenvironmental Engineering*. 2013

Lam WK, Tatsuoka F. Effects of initial anisotropic fabric and sigma 2 on strength and deformation characteristics of sand. *Soils and Foundations*. 1988; **28**(1): 89–106

Lanier J, Di Prisco C, Nova R. Etude exprimentale et analyse thorique de l'anisotropie induite du sable Hostun. Revue Francaise de *Gotechnique*. 1993; **57**: 59–74

Li X, Yu HS, Li XS. A virtual experimental technique on the elementary behavior of granular materials with discrete element method. *Intern. Journ. Numer. Anal. Meth. Geomech.* 2013; **37**(1): 75–96.

Li XS, Dafalias Y F. Constitutive modeling of inherently anisotropic sand behavior. *Geotech. Geoenviron. Eng*. 2002; **128**(10): 868–880

Matsuoka H, Sakakibara K. A constitutive model for sands and clays evaluating principal stress rotation. *Soils and Foundations.* 1987; **27**(4): 73–88.

Mitchell RJ. Some deviations from isotropy in lightly overconsolidated clay.

Geotechnique. 1972; **22**: 459–467.

Mroz Z. On the description of anisotropic work hardening. *J. Mech. Phys. Solids*. 1967; 15: 163–175.

Nova, R. (1980). The failure of transversely anisotropic rocks in triaxial compression. *Intern. Journ. Rock Mech Min. Sci.* 1980; **17**(3): 25–32.

O'Sullivan C. Particulate Discrete Element Modelling: A Geomechanics Perspective. *Taylor and Francis*. 2011

Oda M, Koishikawa I, Higuchi T. Experimental study of anisotropic shear strength of sand by plane strain test. *Soils and Foundations* 1978; **18**(1): 25–38.

Oda M, Koishikawa I. Anisotropic fabric changes during compressinal deformation of sand. *Soils and Foundations*; **12**(2): 1–18

Oda M, Nemat-Nasser S, Konishi J. Stress-induced anisotropy in granular masses. *Soils and Foundations.* 1985; **25**(3), 85–97.

Oda M, Nemat-Nasser S, Konishi J. Stress-induced anisotropy in granular masses*, Soils and Sounds*. 1985; **25** (3), 85–97

Oda M. The mechanism of fabric changes during compressional deformation of sand. *Soils Found*. 1972; **14**:1–18

Oka F, Kimoto S, Kobayashi H, Adachi T. Anisotropic behavior of soft sedimentary rock and a constitutive model. *Soils and Foundations*. 2002; 42(5): 59–70

Pande GN, Sharma KG. Multi-laminate model of clays- A numerical evaluation of the

influence of rotation of the principal stress axes. *International Journal for Numerical and Analytical Methods in Geomechanics*. 1983; **7**: 397–418

Pande GN, Xiong W. An improved multilaminate model of jointed rock masses." *Proc., Int. Symp. on Numer. Models in Geomech*., Dungar R, GN Pande, GA Studer, eds., Balkema, Rotterdam, The Netherlands. 1982; 218–226.

Pande, GN, Sharma KG Time-dependent multilaminate model for clay—A numerical study of the influence of rotation of principal stress axes. *Proc., Implementation of Computer Procedures and Stress–Strain Laws in Geotech. Engrg.* 1981; **2**, Acorn Press, Durham, NC: 575–590.

Pariseau, W. Plasticity theory for anisotropic rocks and soils. *Proceedings 10th Symposium on Rock Mechanics, AIME.* 1972.

Pietruszczak S, Guo P. Description of deformation process in inherently anisotropic granular materials. *Int. J. Numer. Anal. Meth. Geomech.* 2013*;* **37***:*478–490.

Pietruszczak S, Mroz Z. Formulation of anisotropic failure criteria incorporating a microstructure tensor. *Comp. Geotech*. 2000; **26**: 105–112.

Pietruszczak S, Mroz Z. On failure criteria for anisotropic cohesive frictional materials . *Intern. Journ. Numer. Anal. Meth. Geomech*. 2001; **25***:* 509–524.

Pietruszczak S. Fundamentals of plasticity in geomechanics. *McMaster University, Hamilton, Ontario, Canada*. 2010

Pietruszczak S, Krucinski S. Description of anisotropic response of clays using a tensorial measure of structural disorder. *Mechanics of Materials*. 1989; **8**(23): 237–249.

Pietruszczak S, Lydzba D, Shao JF. Description of creep in inherently anisotropic frictional materials, *J Eng. Mech*. 2004; **130**(6): 681-690

Pietruszczak S, Pande GN Description of soil anisotropy based on multi-laminate framework. *Int. J. Numer. Analyt. Meth. Geomech*. 2001; **25**(2): 197–206.

Poorooshasb HB, Holubec I, Sherbourne AN. Yielding and flow of sand in triaxial compression: part 2 and 3. *Can Geotech J*. 1967; **4**(4): 376–397

Poorooshasb HB, Holubec I, Sherbourne AN. Yielding and flow of sand in triaxial compression: part 1. *Can Geotech J*. 1966; **3**(4): 179–190

Prevost JH. Mathematical modeling of monotonic and cyclic undrained clay behavior. *Int. J. Numer. Analyt. Meth. Geomech*. 1977; **1**: 195–216

Prevost JH. Plasticity theory for soil stress–strain behavior. *J. Engrg. Mech.* 1978; **104**(5): 1117–1194

Prevost JH. Two-surface versus multi-surface plasticity theories: A critical assessment. *Int. J. Numer. Analyt. Meth. Geomech*. 1982; **6**: 323–328

Roscoe KH, Arthur JRF, James RJ. The determination of strains in soils by an X-ray method. *Civ. Eng. Publ.* 1963; **58**: 873–876

Rothenburg L, Bathurst RJ. Micromechanical features of idealized of granular assemblies with planar elliptical particles. *Geotechnique*. 1992; **42** (l), 79–95

Roux JN. Geometric origin of mechanical properties of granular materials. *Physical Review E.* 2000; **61**(6): 6802-6836.

Saada AS, Bianchini GF, Liang L. Cracks, bifurcation and shear bands propagation in saturated clays. *Geotechnique*. 1994; **44**(1): 35–64

Saada AS. Laboratory testing for the validation of constitutive models, in: Modeling in Geomechanics, Eds. Zaman, Gioda and Booker, *John Wiley & Sons, LTD*. 2000

Saada AS. State-of-the-art: Hollow cylinder torsional device: their advantage and limitations. *Advanced Triaxial testing of Soils and Rocks,* ASTM STP977, Philadelphia, PA. 1988; 766–795.

Schultz T, Kindlmann GL. Superquadric glyphs for symmetric second order tensors. *IEEE Trans. Visual. Comp. Graph.* 2010; **16**(6): 1595–1604.

Sivathayalan S, Vaid YP. Influence of generalized initial state and principal stress rotation on the undrained response of sands. *Can Geotech J.* 2002; **39**(1): 63–76

Symes MJPR, Gens A, Hight DW. Drained principal stress rotation in saturated sand *Geotechnique.* 1988; **38**(1): 59–81

Symes MJPR, Gens A, Hight DW. Undrained anisotropy and principal stress rotation in saturated sand. *Geotechnique*. 1984; **34**(l): 11–27

Tatsuoka F, Ishihara K. Yielding of sand in triaxial compression. *Soils Found*. 1974; **14**(2): 63–76

Tsai SW, Wu E. A general theory of strength of anisotropic materials. *Journ. Comp. Mat.* 1971*;* **5**: 58–80.

Vaid YP, Chung EKF, Kuerbis RH. Pre-shearing and undrained response of sands. *Soils Found*. 1989; **29**(4): 49–61

Vaid YP, Sayao ASF, Hou E, Negussey D. Generalized stress path dependent soil behavior with a new hollow cylinder torsional apparatus. *Can Geotech J*. 1990; **27**(5): 601–616

Walsh JB, Brace JF. A fracture criterion for brittle anisotropic rock. *Journal of Geophysical Research*. 1964; **69**: 3449–3456.

Wang L, Frost J, G ZVoyiadjis, Harman T. Quantification of damage parameters using X-ray tomography images. *Mech. Mater.* 2002; **35**: 777–790.

Whitehouse W. The quantitative morphology of anisotropic trabecular bone. *Journ. Microscopy.* 1974; **101**(2): 153–168.

Wong RKS, Arthur JRF. Induced and inherent anisotropy in sand. *Geotechnique*. 1985; **35**: 471–481

Yamada Y, Ishihara K. Anisotropic deformation characteristics of sand under three dimensional stress conditions. *Soils and foundations*. 1979; **19**(2): 79–94

Yang ZX, Li XS, Yang J. Undrained anisotropy and rotational shear in granular materials. *Geotechnique*. 2007; **57**(4): 371–384

Zienkiewicz OC, Pande GN. Time-dependent multilaminate model of rocks—A numerical study of deformation and failure of rock masses." *Int. J. Numer. Analyt. Meth. Geomech*. 1977; **1**: 219–247.